Lithos 318–319 (2018) 124–142

Contents lists available at ScienceDirect

Lithos

journal homepage: www.elsevier.com/locate/lithos

Petrology and geochemistry of mafic and ultramafic rocks in the north Tianshan ophiolite: Implications for petrogenesis and tectonic setting

Wanyi Feng, Yongfeng Zhu *

Key Laboratory of Orogenic Belts and Crustal Evolution, School of Earth and Space Science, Peking University, Beijing 100871, China

ARTICLE INFO

Article history:
Received 11 February 2018
Accepted 8 August 2018
Available online 10 August 2018

Keywords:
Ophiolite
Serpentinized harzburgite
Serpentinite
Basalt
North Tianshan

ABSTRACT

New petrological and geochemical data for the mafic (pillow basalt, massive basalt, gabbro) and ultramafic rocks (serpentinite, serpentinized harzburgite) in the north Tianshan ophiolite cropping out along the Duku road are combined to constrain the geological evolution of the north Tianshan ophiolite, which marks the boundary between the Yili-central Tianshan and the Junggar terranes. Pillow basalt, characterized by significant enrichments of light rare earth elements (REE) as well as high Nb/Yb and TiO_2/Yb ratios, probably represents the seamount fragments accreting in the north Tianshan accretionary prism. Massive basalt and gabbro, displaying flatten REE patterns with low Ti/V ratios, are similar to forearc basalts. Serpentinite and serpentinized harzburgite, belonging to the mantle section of the ophiolite, are depleted in incompatible elements compared to the primitive mantle. The compositions of primary chromian spinel, olivine, and pyroxene in these mantle rocks are comparable to those in forearc peridotites. Such characteristics indicate that the protoliths of serpentinite and serpentinized harzburgite have undergone high degrees of partial melting. They were modified by island arc tholeiitic to boninitic melts during and/or after melt extraction as suggested by the enrichment of Ti in chromian spinel coupled with the occurrence of amphibole inclusions in chromian spinel. These new petrological and geochemical data suggest that the north Tianshan ophiolite was generated in a forearc setting. Retreat and rollback of the north Tianshan subducted slab triggered the upwelling of asthenosphere with minor mass transfer from the slab, leading to the formation of massive basalt and gabbro. Increasing flux of slab-derived fluids/melts largely enhanced partial melting degree of the mantle peridotites, producing island arc tholeiitic to boninitic melts. These melts interacted with refractory mantle residues and formed the mantle rocks (i.e., the protoliths of serpentinite and serpentinized harzburgite) in the north Tianshan ophiolite.

1. Introduction

Ophiolites are the remnants of fossil oceanic lithosphere that were tectonically emplaced onto continental margins and can provide useful information to reconstruct the magmatic and tectonic history of the oceanic lithosphere (Dilek and Furnes, 2011). Although ophiolites can be generated in different tectonic settings, such as continental margin, mid-ocean ridge and plume-related settings, the vast majority is now proposed to form in a supra-subduction-zone environment (Shervais, 2001; Stern et al., 2012; Uysal et al., 2016; Zhu and Ogasawara, 2002). Recognition of most ophiolites as a forearc origin is mainly based on the occurrence of forearc basalt, island arc tholeiite ± boninite (Dilek et al., 2007; Reagan et al., 2010; Saccani et al., 2017) as well as highly refractory mantle rocks displaying typical U-shaped REE patterns (Marchesi et al., 2016; Morishita et al., 2011; Saka et al., 2014).

The north Tianshan accretionary complex (NTAC) marks the final collision between the Yili-central Tianshan and Junggar terranes following the closure of the north Tianshan or Junggar ocean (Fig. 1a), one branch of the Paleo-Asian ocean (Han et al., 2010; Zhu et al., 2016). The north Tianshan ophiolite constitutes the major part of the NTAC. The genetic mechanism and tectonic setting of this ophiolite remain controversial. Xia et al. (2005) suggested that the north Tianshan ophiolite formed in a rift setting due to the presence of OIB-type volcanic rocks, while some authors claimed that it represents the remnants of oceanic crust and seamount developed on the north Tianshan ocean (Chen et al., 2012; Yang et al., 2018). Additionally, Li et al. (2015) argued that the MORB, OIB, and island arc geochemical characteristics displaying in the crustal rocks in the north Tianshan ophiolite were likely related to the subduction of spreading ridges. These conclusions were reached largely based on systematic geochemical studies on the crustal rocks in the north Tianshan ophiolite. However, the mantle rocks in the north Tianshan ophiolite have not been well documented, and the genetic link between the mantle and the crustal rocks is poorly understood. Here we present detailed geological, mineralogical, and whole-rock geochemical data for the mafic and ultramafic rocks in the north Tianshan ophiolite cropping out along the Duku road. These data, together with those from the literature are used to characterize

* Corresponding author.
E-mail address: yfzhu@pku.edu.cn (Y. Zhu).

https://doi.org/10.1016/j.lithos.2018.08.012
0024-4937/

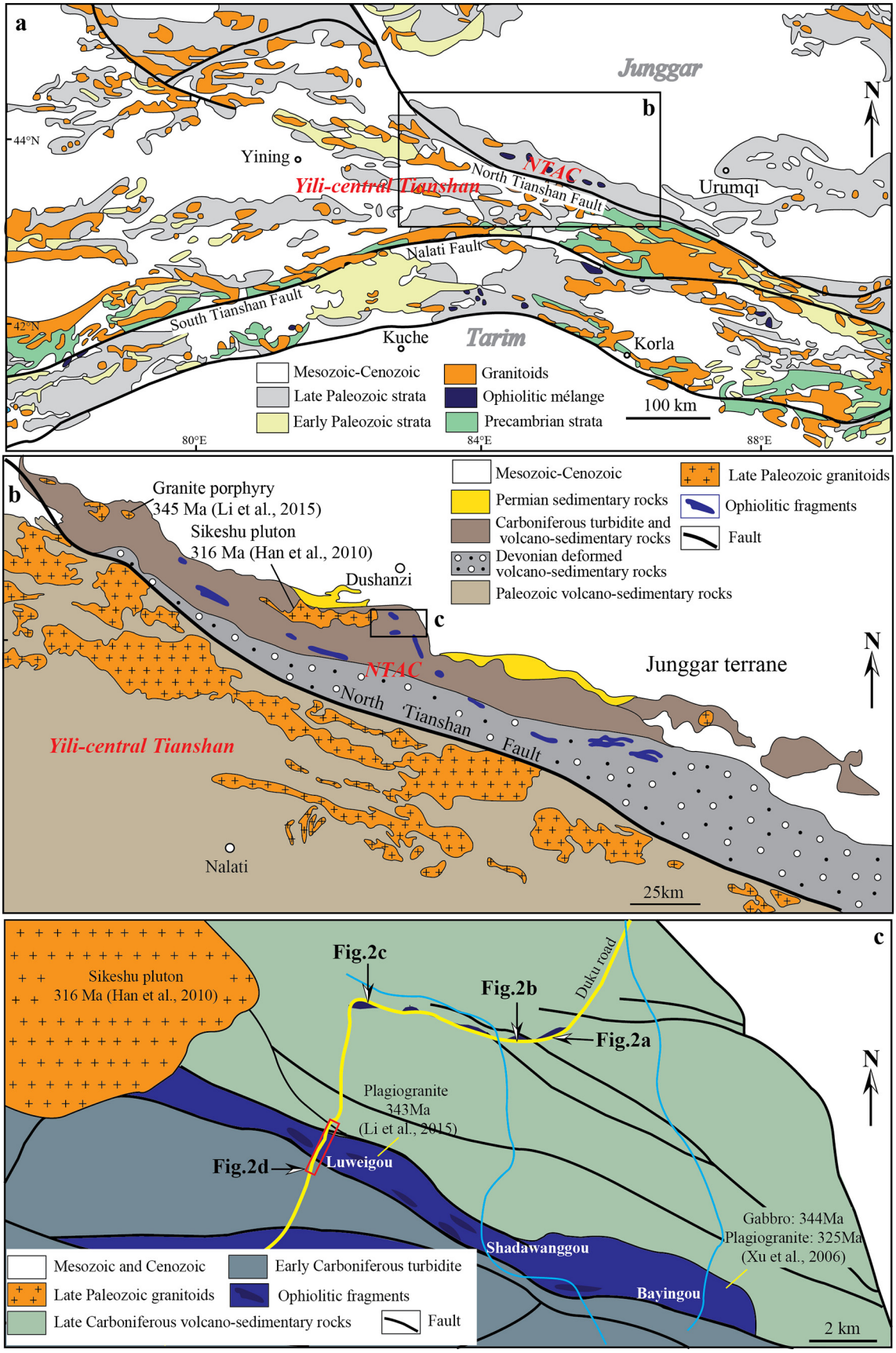

Fig. 1. (a) Geological map of Chinese west Tianshan and adjacent regions (modified after Zhang et al., 2017). Abbreviation: NTAC, north Tianshan accretionary complex. (b) Geological map of the NTAC and adjacent regions (modified after Han et al., 2010). (c) Geological map showing the distribution of the north Tianshan ophiolite (modified after Wu and Liu, 1989).

the mantle rocks and various crustal rocks in the north Tianshan ophiolite. The main objectives of this paper are to elucidate the origin of the mantle and the mafic rocks in the north Tianshan ophiolite, and to provide an explanation for these rocks in a regional geodynamic framework.

2. Geological background

The NTAC (Fig. 1a), located between the Yili-central Tianshan and the Junggar terranes was generated by the southward subduction of the north Tianshan ocean during late Paleozoic era (An et al., 2017; Han et al., 2010; Zhang et al., 2017; Zhu et al., 2005). It is bounded by the northwest-striking north Tianshan fault in the south and a series of north-directed thrust faults in the north. This accretionary complex predominantly consists of two different lithologies: Devonian-Carboniferous volcano-sedimentary rocks and ophiolitic remnants (Wang et al., 2006; Fig. 1b). Devonian volcano-sedimentary rocks, which underwent low-grade metamorphism and deformation are widely distributed along the north Tianshan fault. They are mainly composed of tuffaceous sandstone, tuff, slate, phyllite, limestone, and intermediate-mafic volcanic rocks. The lower Carboniferous sequence, estimated to be 5000–10,000 m thick, is dominated by black rhythmic tuffaceous siltstones (An et al., 2013; Zhu et al., 2009). This unit was interpreted as a flysch unconformably overlying the north Tianshan ophiolite. Some shallow-water fossils of crinoids and brachiopods were found in the limestone breccias interbedded within rhythmic tuffaceous siltstones (Chen et al., 2015). The lower Carboniferous sequence is unconformably overlain by the Late Carboniferous clastic and pyroclastic rocks. Permian terrestrial sandstone, conglomerate, and volcanic rocks related to post-collisional processes locally overlie the NTAC with angular discontinuity (Fig. 1b).

The north Tianshan ophiolite crops out discontinuously for about 200 km long (Fig. 1b). These ophiolitic rocks mainly consist of serpentinite, serpentinized harzburgite, gabbro, plagiogranite, massive basalt, pillow basalt as well as pelagic sediments (Li et al., 2015; Wu and Liu, 1989; Xia et al., 2005). They typically occur as thrust slices and blocks within the Devonian to Carboniferous volcano-sedimentary rocks (Figs. 1b-c). Early Carboniferous radiolarians were found in chert (Xiao et al., 1992). Plagiogranite and gabbro from the Bayingou region were dated to be 324.8 ± 7.1 Ma and 344.0 ± 3.4 Ma, respectively (Fig. 1c; Xu et al., 2006), while plagiogranite from the Luweigou region yielded zircon U—Pb ages of 343.1 ± 2.7 Ma (Fig. 1c; Li et al., 2015). Undeformed granitic plutons with emplacement ages ranging from 316 Ma to 345 Ma have been identified in the NTAC (Fig. 1b; Han et al., 2010; Li et al., 2015).

Serpentinite and serpentinized harzburgite are distributed discontinuously along the Duku road between the Luweigou and the Bayingou regions (Fig. 1c). They are in fault contact with siltstone (Figs. 2a-c, 3a, b, d) or occur as lenses in serpentinite (Fig. 3c). Gabbro and basalt are exposed in the Luweigou region (Fig. 1c). They are generally in fault contact with each other (Figs. 2d, 3e). Sample locations are shown in Fig. 2. Serpentinite samples (F1, F2, F7 to F18) were collected from section I (Fig. 2a), of which samples F10 and F11 contain some oval-shaped serpentinite lenses (Fig. 3c). Serpentinized harzburgites were sampled from section II and section III (Figs. 2b-c), including samples F27, 16F82, 16F83, 16F85, 16F86, and 16F87. Gabbroic samples (16F90 to

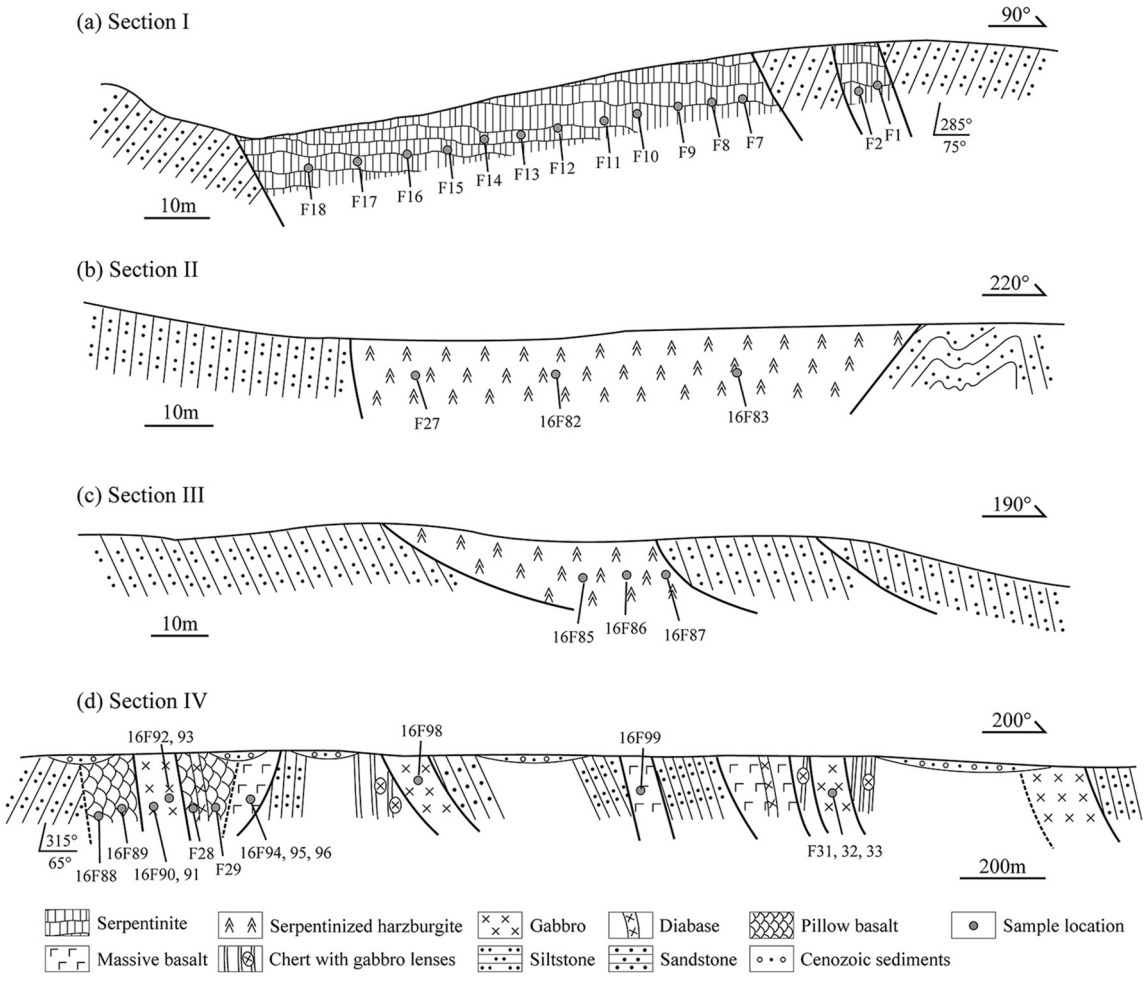

Fig. 2. Four geological sections showing sample locations of the north Tianshan ophiolite along the Duku road.

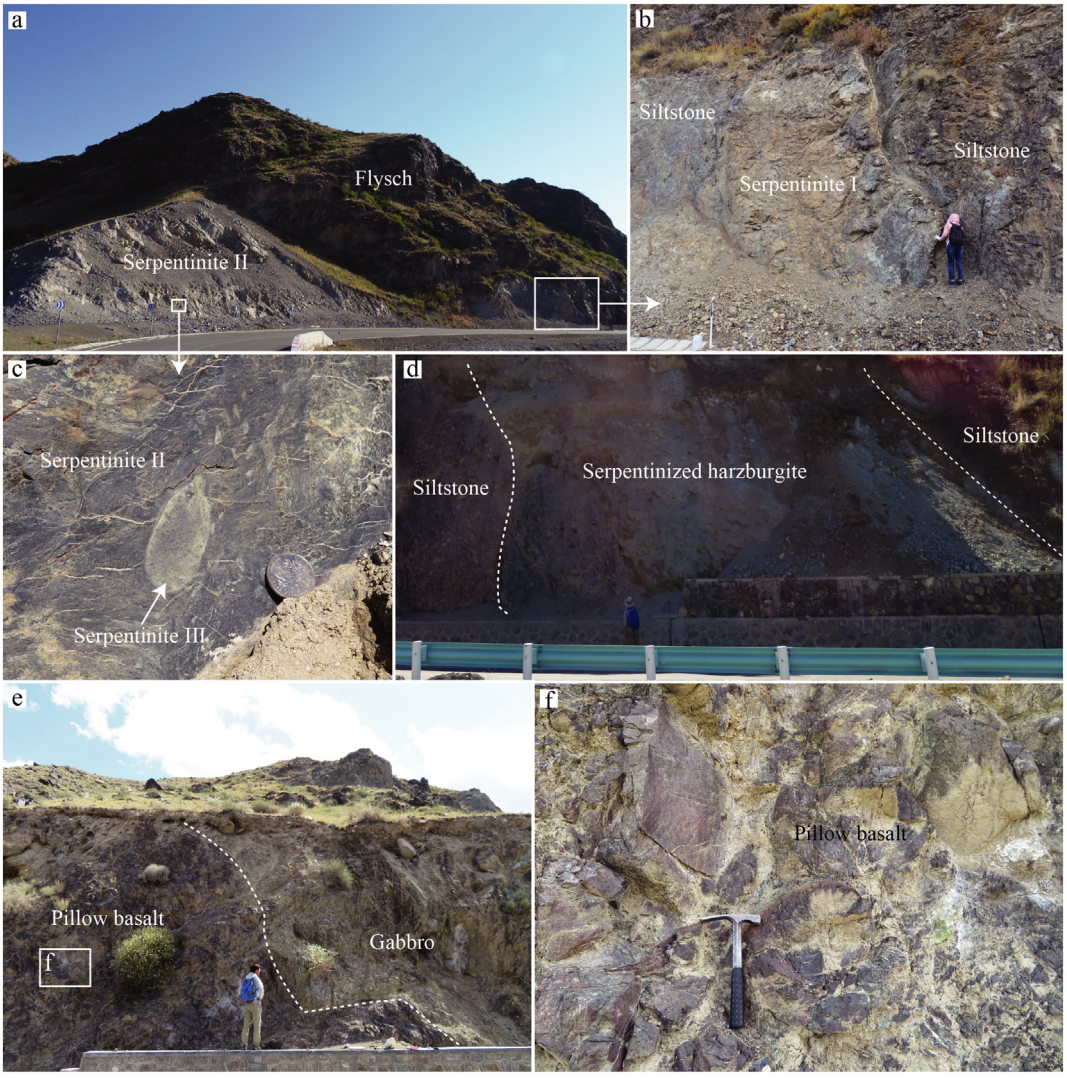

Fig. 3. Field photographs of the north Tianshan ophiolite. (a) Field outcrop of serpentinites. (b) Serpentinite I in fault contact with siltstone. (c) Oval-shaped serpentinite III hosted in the serpentinite II. (d) Serpentinized harzburgite in fault contact with siltstone. (e) Pillow basalt and gabbro showing a fault contact relationship. (f) Pillow basalt in the field.

16F93, 16F98, F31 to F33), massive basaltic samples (16F94, 16F95, 16F96, 16F99), and pillow basaltic samples (F28, F29, 16F88, 16F89) were collected from section IV (Fig. 2d).

3. Laboratory methods

The chemical compositions of mineral phases were measured by electron probe microanalysis (EPMA) using a JEOL JXA-8230 electron microprobe equipped with four wavelength dispersive spectrometers. An acceleration voltage of 15 kV and a beam current of 10 nA were used for all analyses. The beam diameter was set at 1–2 μm, and counting times of 20 s were used for both peak and background. The following standards (from SPI corp. US) were adopted for various elements: sanidine (K), diopside (Ca, Mg), rutile (Ti), jadeite (Na, Al, Si), chromium oxide (Cr), rhodonite (Mn), hematite (Fe), and nickel silicide (Ni). Final results were corrected using the PRZ method. Detection limits of the oxides were 0.01 wt% for K_2O, 0.02 wt% for Al_2O_3 and Na_2O, 0.03 wt% for MgO and CaO, 0.04 wt% for TiO_2, Cr_2O_3, MnO, FeO, and NiO, and 0.06 wt% for SiO_2.

The selected samples were washed by distilled water, and then milled in an agate mortar to about 200 meshes for whole rock analysis. The whole rock powder was made into glass discs by fusion with lithium metaborate. Measurement of major elements as well as Ni, Cr, and V was done by X-ray fluorescence (XRF) spectrometry on glass. Rb, Ba, Th, U, Zr, Hf, Nb, Ta, Y, and REE were determined by Agilent 7500 inductively coupled plasma mass (ICP-MS) spectrometer. Standard samples DZS-1, GSR-3, and GSR-10 were used for calibration. The results of our calibration analyses consistently compared well with the reference values (e.g., the recommended Ba, La, and Yb values of DZS-1 were 6.40 ppm, 0.20 ppm, and 0.020 ppm, respectively; our measured Ba, La, and Yb contents were 6.54 ppm, 0.19 ppm, and 0.021 ppm, respectively). This quality control demonstrated that the measurement error of our analyses was <10% for most trace elements, with the exception of Eu (21%), Ho (17%), and Y (16%). Relative to GSR-3 and GSR-10, the accuracy of our analyses for all trace elements was <10% deviation from true values. Detection limits of trace elements (in ppm) were: Ba, Zr, Nb = 0.02; La, Y = 0.004; Ce, Rb, Ta, Hf = 0.003; Dy, Er, Ta = 0.002; Nd, Sm, Yb = 0.001; Pr, Eu, Gd, Tb, Ho, Tm, Lu, Th, U = 0.0006.

4. Results

4.1. Petrography

Massive basalt is porphyritic with phenocrysts of plagioclase and clinopyroxene. Plagioclase phenocrysts (~ 2 vol%) generally show tabular euhedral forms and range from 0.2 mm to 0.6 mm in length. Clinopyroxene phenocrysts (~ 1 vol%) are euhedral to subhedral with sizes ranging from 0.2 mm to 0.7 mm. The groundmass is mainly

composed of fine-grained plagioclase, clinopyroxene, and cryptocrystalline minerals. Pillow basalt typically shows pillow structure (Fig. 3f) and porphyritic texture with phenocrysts of plagioclase and clinopyroxene embedded in the groundmass consisting of plagioclase, clinopyroxene, and cryptocrystalline minerals. Plagioclase phenocrysts (2–4 vol%) are euhedral with sizes ranging between 0.4 mm and 3.5 mm, whereas clinopyroxene phenocrysts (~ 1 vol%) are euhedral to subhedral with sizes ranging from 0.2 mm to 0.5 mm.

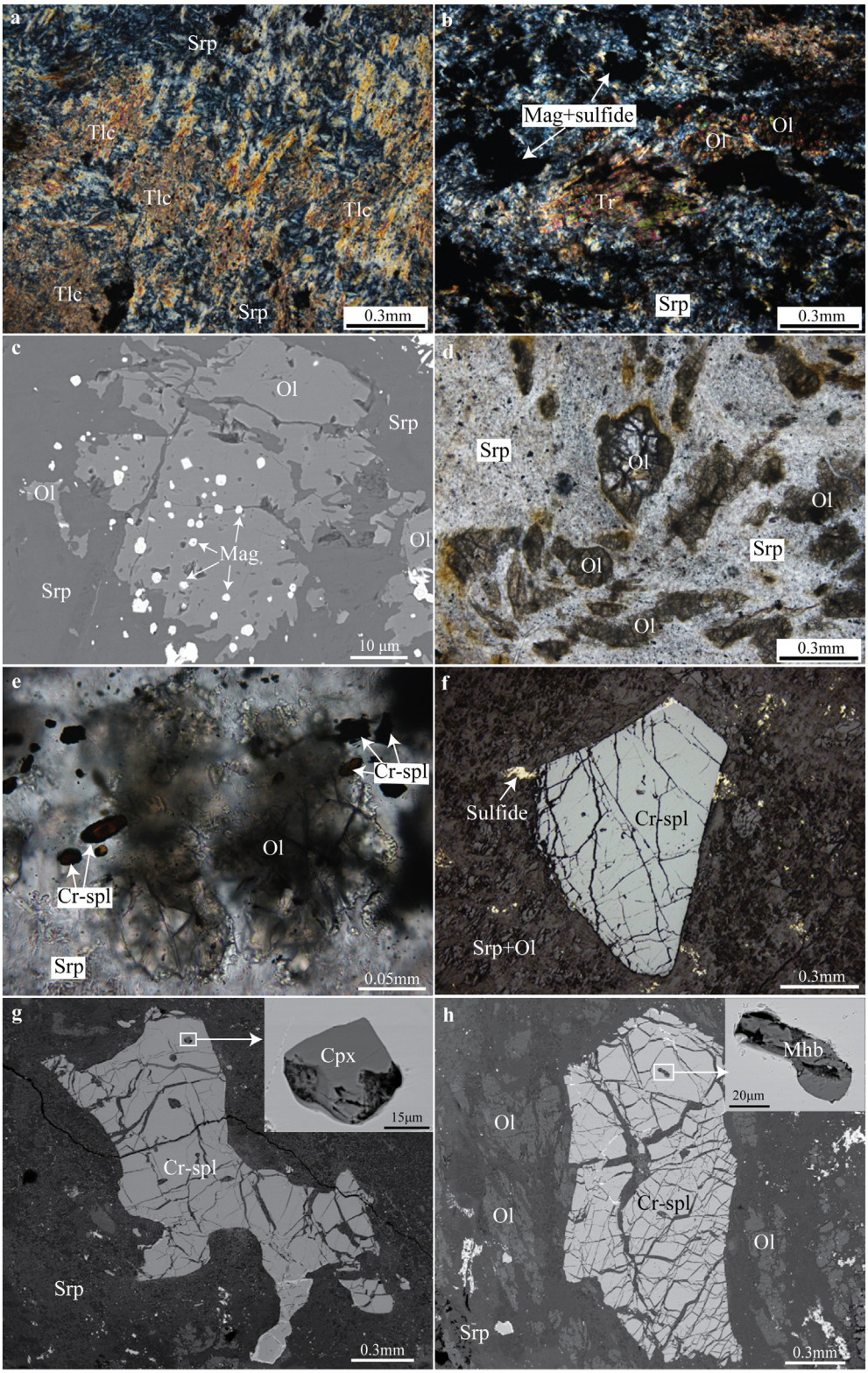

Fig. 4. Photomicrographs of serpentinite I in the north Tianshan ophiolite. (a) The serpentine is replaced by talc, cross-polarized light. (b) Fine-grained olivine, tremolite, magnetite, and sulfides distributing in the serpentine matrix, cross-polarized light. (c) Magnetite occurs as tiny inclusions in the fine-grained olivine, back scattered electron (BSE). (d) Brownish, fine-grained olivine embedded in the serpentine matrix, single-polarized light. (e) Brownish, fine-grained olivine and its surrounding small Cr-spinel grains, single-polarized light. (f) A euhedral Cr-spinel grain, reflected light. (g) An anhedral Cr-spinel grain with a clinopyroxene inclusion, BSE. (h) An elongated Cr-spinel grain with an amphibole inclusion, BSE. Abbreviations: Srp, serpentine; Tlc, talc; Ol, olivine; Tr, tremolite; Mag, magnetite; Cr-spl, Cr-spinel; Cpx, clinopyroxene; Mhb, magnesiohornblende.

Gabbro is typically massive with ophitic or poikilitic texture. It is mainly composed of plagioclase (~ 50 vol%), clinopyroxene (42–45 vol %), and minor Fe—Ti oxides (5–8 vol%). Plagioclase (0.3–1.5 mm in length) usually occurs as tabular subhedral to euhedral laths. Clinopyroxene (0.5–2 mm in size) is subhedral to anhedral in shape and replaced by amphibole in some cases. Fe—Ti oxides (0.1–0.4 mm in size) generally fill interstices between plagioclase and clinopyroxene.

The mantle rocks in the north Tianshan ophiolite could be classified into four groups: serpentinite I, serpentinite II, serpentinite III, and serpentinized harzburgite.

Serpentinite I (samples F1 and F2) consists of serpentine, talc, olivine, and chromian spinel (Cr-spinel) with minor tremolite, magnetite, and sulfides (Fig. 4). Trace amounts of zircon were also found in these samples. Serpentine usually occurs as fine-grained lepidoblastic aggregates and is typically replaced by talc (Fig. 4a). Tremolite occurs as randomly oriented slender prisms (Fig. 4b). Magnetite and sulfides occur as finely dispersed grains and elongated strings in the serpentine matrix (Fig. 4b), or as inclusions in olivine (Fig. 4c). Olivine (20–25 vol%) grains are fractured and sheared (Fig. 4d). They are generally brownish in color with sizes <0.5 mm and contain numerous opaque inclusions (Figs. 4c-e), which are similar to the metamorphic olivine in thermally metamorphosed serpentinites (Nozaka, 2003). Cr-spinel (~3 vol%) shows a bimodal grain-size distribution in these samples, exhibiting relatively small grains (<0.15 mm; Fig. 4e) and large grains (1–1.5 mm; Figs. 4f–h). The smaller Cr-spinel grains heterogeneously distribute around olivine grains (Fig. 4e), while the larger ones are generally euhedral to anhedral in shape (Fig. 4f–h). Most of Cr-spinel grains are replaced by chromian magnetite along fractures and grain boundaries. Olivine, clinopyroxene (Fig. 4g), and amphibole (Fig. 4h) were found in the Cr-spinel as inclusions.

Serpentinite II (samples F7 to F18) has been overprinted by intense shear deformation (Fig. 5a), which obscures its exact modal

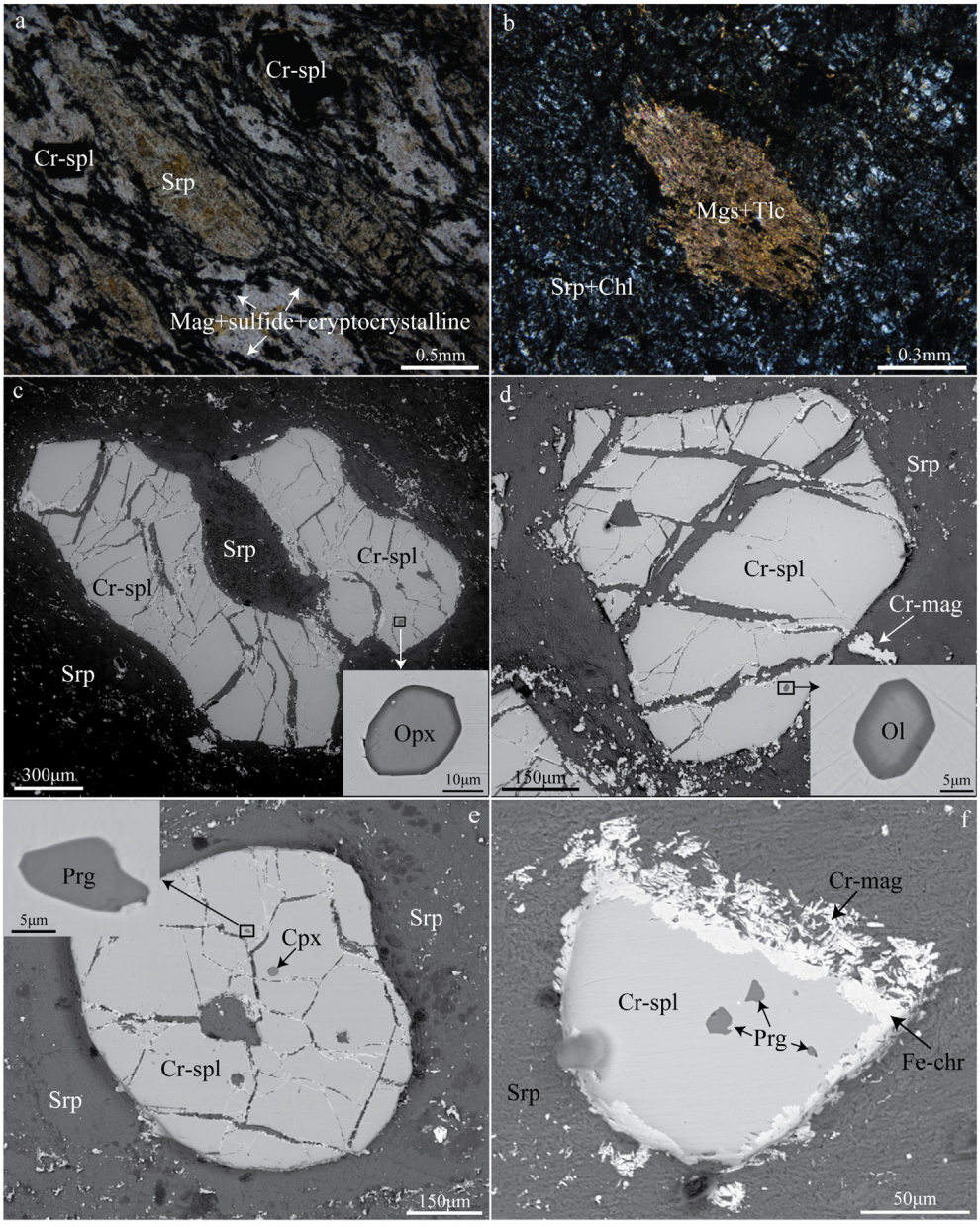

Fig. 5. Photomicrographs of serpentinite II in the north Tianshan ophiolite. (a) Serpentinite II displaying a mylonitic texture, single-polarized light. (b) Talc and magnesite embedded in the matrix of serpentine and chlorite, cross-polarized light. (c) Anhedral Cr-spinel grains with an orthopyroxene inclusion, BSE. (d) A euhedral Cr-spinel grain with an olivine inclusion, BSE. (e) A rounded Cr-spinel grain with pargasite and clinopyroxene inclusions, BSE. (f) Cr-spinel grain replaced by ferrian chromite along the margin, BSE. Abbreviations: Cr-spl, Cr-spinel; Srp, serpentine; Chl, chlorite; Tlc, talc; Mgs, magnesite; Fe-chr, ferrian chromite; Cr-mag, chromian magnetite; Opx, orthopyroxene; Ol, olivine; Cpx, clinopyroxene; Prg, pargasite.

mineralogical compositions and primary textures. In addition to serpentine, other altered silicate phases include chlorite and trace amounts of talc and magnesite (Fig. 5b). Base-metal minerals include magnetite and minor sulfide grains, generally forming elongated strings within the serpentine matrix. Variable amounts of cryptocrystalline minerals that formed during mylonitization were also observed in the studied samples (Fig. 5a). Cr-spinel (3–4 vol%) with various shapes (Fig. 5c–f) is the only fresh mineral preserved in serpentinite II samples. Most Cr-spinel grains are cataclastically broken and fractured, and typically rimmed by chromian magnetite ± ferrian chromite overgrowths (Fig. 5f). Olivine, pyroxene, and amphibole are hosted in Cr-spinel grains as inclusions (Fig. 5c–f).

Serpentinite III refers to the oval-shaped serpentinite lenses hosted in serpentinite II (Figs. 3c, 6a; samples F10 and F11). Compared to serpentinite II, serpentinite III contains slightly higher proportions of Cr-spinel (~ 5 vol%), but without talc and magnesite. Moreover, serpentinite III does not display mylonitic textures as shown in serpentinite II (Fig. 6b). Serpentine in serpentinite III typically exhibits interpenetrating textures (Fig. 6c) and none of pseudomorphic crystals are preserved. Cr-spinel (0.3–0.8 mm in size) commonly displays euhedral isometric morphologies with embayed or roundish cores surrounded by ferrian chromite (inner rim) to porous chromian magnetite (outer rim) (Fig. 6d). These cores usually contain olivine (Fig. 6e) and amphibole inclusions (Fig. 6f).

Serpentinized harzburgite contains 70–75 vol% olivine, 20–25 vol% orthopyroxene, < 3 vol% clinopyroxene, and ~ 2 vol% Cr-spinel (Fig. 7a). Olivine grains (0.5–2 mm in size) are free from opaque inclusions and replaced by serpentine with mesh texture (Figs. 7b-d). Orthopyroxene grains (3–6 mm in size) commonly occur as porphyroclasts and occasionally display curved exsolution lamellae of clinopyroxene (Figs. 7e-f). Most orthopyroxene grains have been replaced by bastite (Fig. 7g). Clinopyroxene typically occurs as interstitial phase among olivine and orthopyroxene grains with sizes <0.5 mm (Fig. 7a), indicating its secondary origin. Cr-spinel (< 1.5 mm in size) is euhedral to anhedral in shape (Figs. 7a-d) and contains a few silicate

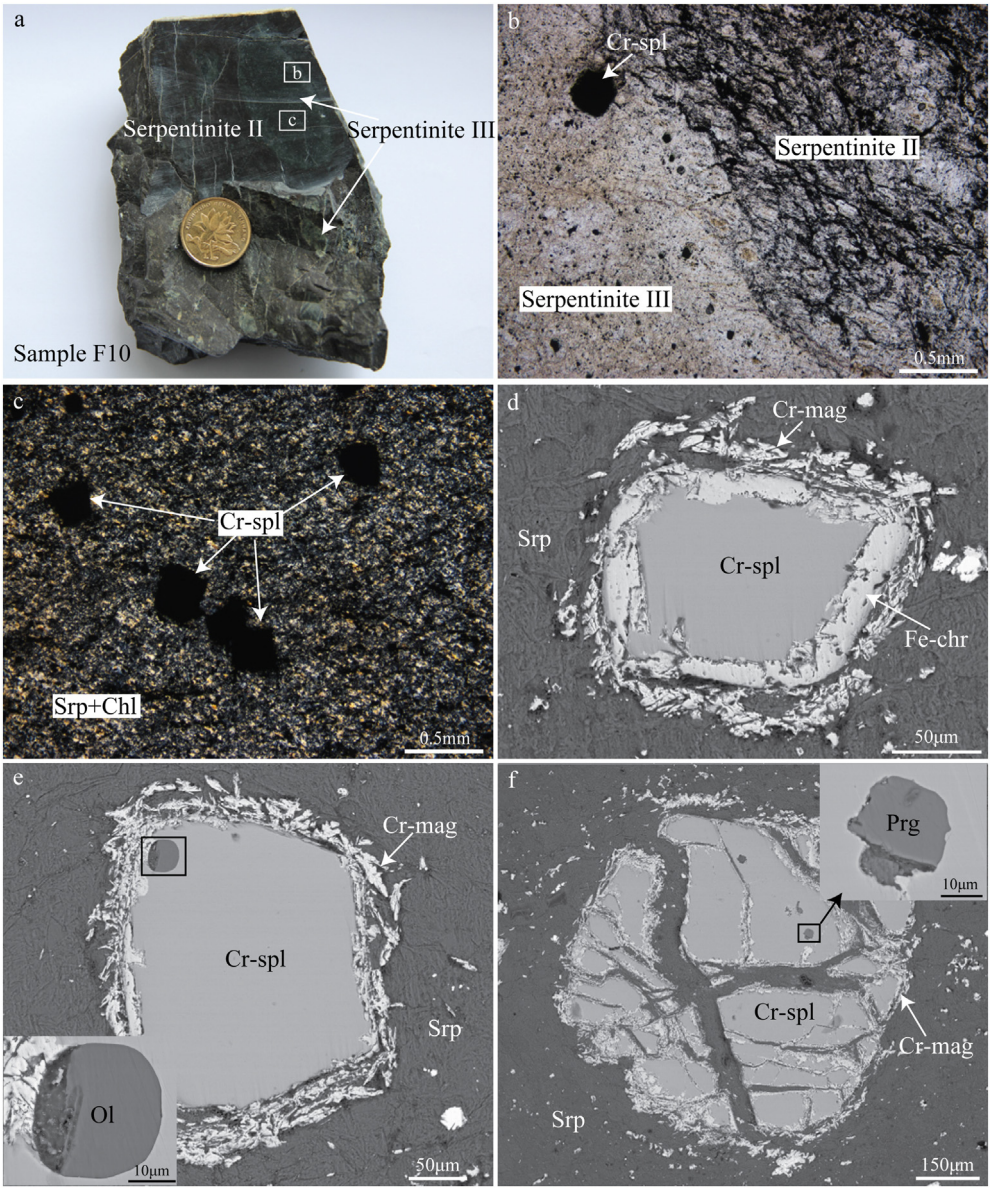

Fig. 6. Photos and photomicrographs of serpentinite III in the north Tianshan ophiolite. (a) Oval-shaped serpentinite III occurring as lenses in the serpentinite II. (b) The boundary between serpentinite II and serpentinite III, single-polarized light. (c) Subhedral Cr-spinel grains embedded in the matrix consisting of serpentine and chlorite, cross-polarized light. (d) A euhedral Cr-spinel grain replaced by ferrian chromite and chromian magnetite along the margin, BSE. (e) A euhedral Cr-spinel grain with an olivine inclusion, BSE. (f) A fractured Cr-spinel grain with a pargasite inclusion, BSE. Abbreviations: Cr-spl, Cr-spinel; Srp, serpentine; Chl, chlorite; Fe-chr, ferrian chromite; Cr-mag, chromian magnetite; Ol, olivine; Prg, pargasite.

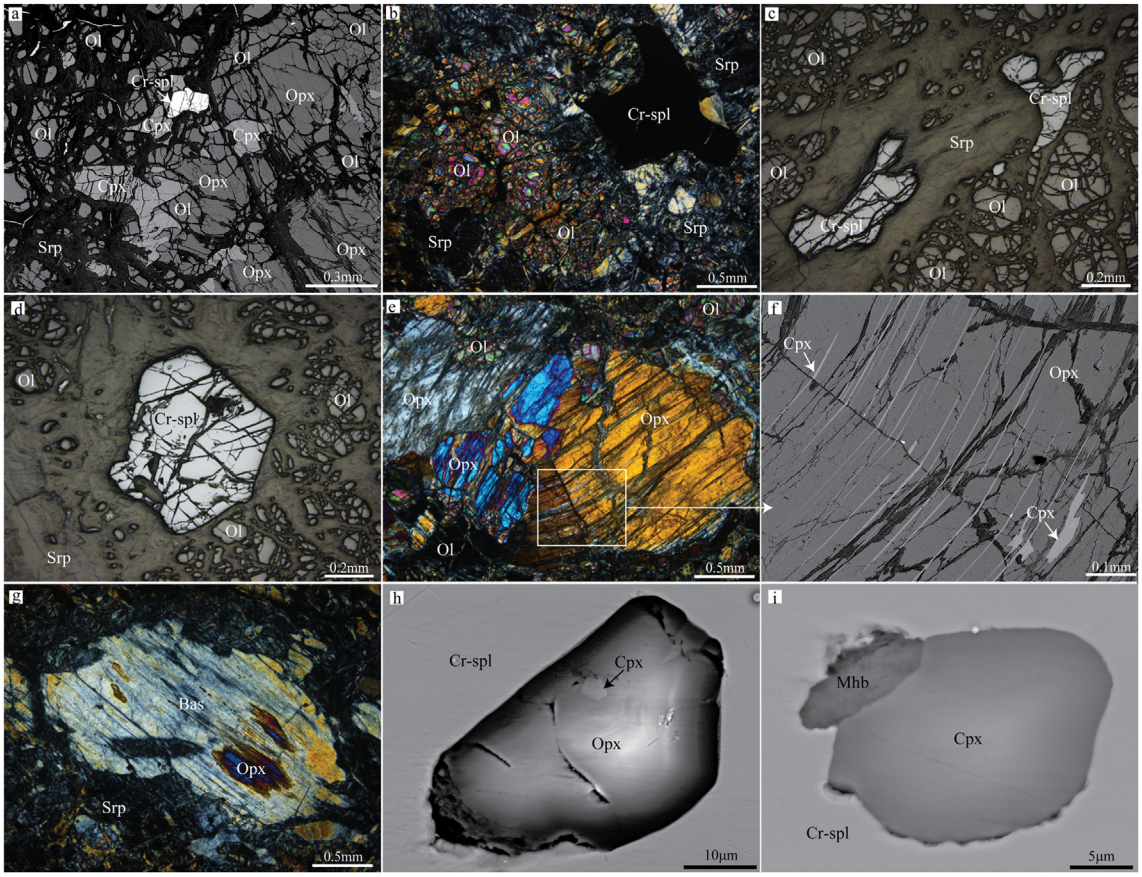

Fig. 7. Photomicrographs of serpentinized harzburgite in the north Tianshan ophiolite. (a) Serpentinized harzburgite mainly consisting of olivine and orthopyroxene with minor clinopyroxene and Cr-spinel, BSE. (b) Anhedral Cr-spinel and partial serpentinized olivine showing a mesh texture, cross-polarized light. (c) Anhedral Cr-spinel and relics of fresh olivine, reflected light. (d) Euhedral Cr-spinel and relics of fresh olivine, reflected light. (e) Orthopyroxene porphyroclast displaying curved exsolution lamellae of clinopyroxene, cross-polarized light. (f) Clinopyroxene occurring as exsolution lamellae in orthopyroxene, BSE. (g) Orthopyroxene is partly altered to bastite, cross-polarized light. (h) An orthopyroxene inclusion in Cr-spinel, BSE. (i) A composite inclusion consisting of magnesiohornblende and clinopyroxene hosted in Cr-spinel, BSE. Abbreviations: Cr-spl, Cr-spinel; Ol, olivine; Opx, orthopyroxene; Cpx, clinopyroxene; Srp, serpentine; Bas, bastite; Mhb, magnesiohornblende.

inclusions (Figs. 7h-i). Cr-spinel is virtually unaltered, and only some grains exhibit thin, ragged coatings of magnetite along fractures.

4.2. Mineral chemistry

Chemical compositions of Cr-spinel, olivine, orthopyroxene, clinopyroxene, and amphibole from various rocks are listed in Supplementary data.

Cr-spinel in the studied rock samples generally shows a homogeneous core with a discontinuous rim. The Cr-spinel rim, composed of ferrian chromite and/or chromian magnetite, represents late-stage alteration processes, and thus only the Cr-spinel core which plots along the Cr—Al join on the Cr-Fe^{3+}-Al diagram (Fig. 8a) is considered here. The compositions of Cr-spinel cores in serpentinite I mainly depend on their grain sizes. The large Cr-spinel grains generally have cores with higher Mg# [$100 \times Mg/(Mg + Fe^{2+})$ atomic ratio; 48–50] but lower Fe^{3+}# [$100 \times Fe^{3+}/(Cr + Al + Fe^{3+})$ atomic ratio; ≤1], Cr# [$100 \times Cr/(Cr + Al)$ atomic ratio; 72–78], and MnO contents (0.34–0.44 wt%) than the small ones (Mg# = 26–43, Fe^{3+}# < 5, Cr# = 81–88, MnO = 0.46–0.69 wt%; Figs. 8b-c). However, all Cr-spinel cores in serpentinite I have similar TiO_2 contents (< 0.10 wt%; Appendix 1a). Cr-spinel cores in serpentinite II have Mg# of 41–50 and Cr# of 74–83. Fe^{3+}#, MnO, and TiO_2 contents of these Cr-spinel cores are ≤5, ≤ 0.50 wt%, and ≤ 0.15 wt%, respectively (Supplementary data 1a). Compared to the Cr-spinel cores in serpentinite II, those in serpentinite III are generally lower in Cr# (52–68) but higher in Mg# (45–61), Fe^{3+}# (1–7), and TiO_2 contents (≤ 0.41 wt%). Cr-spinel cores in serpentinized harzburgite show limited compositional variations (Fig. 8), with Cr# of 54–69, Mg# of 51–59, MnO of 0.17–0.40 wt%, and TiO_2 of ≤0.07 wt %. In general, most analyzed Cr-spinel cores plot in the primary Cr-spinel field on the Cr# vs. MnO diagram (Fig. 8c) with the small Cr-spinel grains in serpentinite I falling in the altered Cr-spinel field. Only the unaltered Cr-spinel would be used to elucidate the petrogenesis and tectonic environment of the studied mantle rocks in the following sections.

The fine-grained olivine in serpentinite I is characterized by low forsterite [Fo = $100 \times Mg/(Mg + Fe_{tot})$ atomic ratio; 84–89] and NiO contents (< 0.20 wt%; Fig. 9a) but high MnO contents (up to 1.22 wt%; Fig. 9b). Combined with the petrological observations (Fig. 4c–e), such compositional fingerprints are in favor of a metamorphic origin for the fine-grained olivine in serpentinite I, which might be formed by the involvement of Fe-rich phases in the dehydration reaction of serpentine (Ahmed and Surour, 2016; Nozaka, 2003). On the other hand, the relict olivine in serpentinized harzburgite and the olivine inclusions in the Cr-spinel are represented by unzoned forsterite with Fo ranging from 90 to 92 and from 92 to 94, respectively (Figs. 9a-b). Both of them have relatively high NiO contents (0.34–0.50 wt%; Fig. 9a) and low MnO contents (< 0.16 wt%; Fig. 9b), and plot in the mantle olivine array on the Fo vs. NiO diagram (Fig. 9a). Compared to the fine-grained olivine in serpentinite I (Cr_2O_3 < 0.09 wt%) and the relict olivine in serpentinized harzburgite (Cr_2O_3 < 0.15 wt%), olivine inclusions are markedly higher in Cr_2O_3 concentrations (0.27–2.33 wt%; Supplementary data 1b), which might be due to the contamination from the host Cr-spinel.

Orthopyroxene analyzed here is composed exclusively of enstatite ($En_{89–92}$ $Fs_{7–9}$ $Wo_{1–3}$; Supplementary data 1c). Relict orthopyroxene in serpentinized harzburgite shows limited compositional variation (Fig. 9c), with Mg# [$100 \times Mg/(Mg + Fe_{tot})$ atomic ratio] of 91–92,

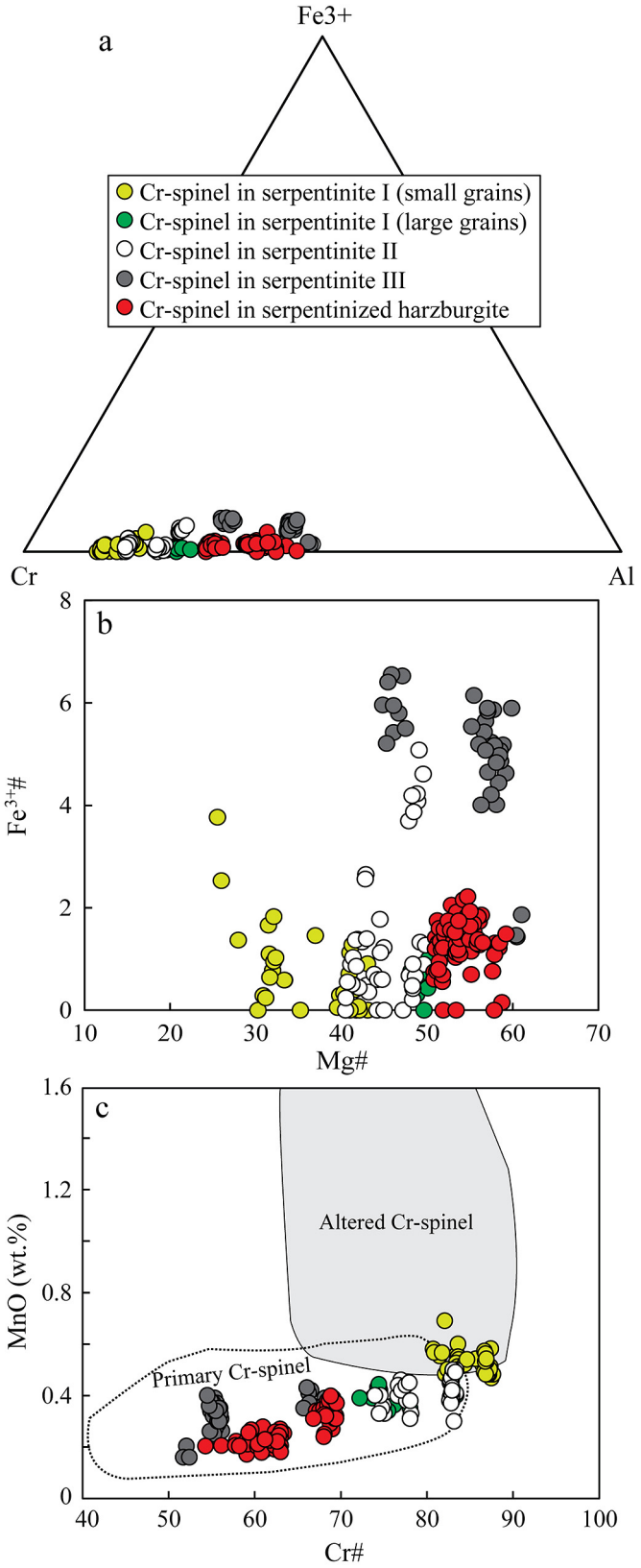

Fig. 8. Compositional variations of Cr-spinel in the mantle rock samples. (a) Cr-Fe^{3+}-Al diagram. (b) Fe^{3+}# [100 × Fe^{3+}/(Cr + Al + Fe^{3+}) atomic ratio] vs. Mg# [100 × Mg/(Mg + Fe^{2+}) atomic ratio] diagram. (c) MnO (wt%) vs. Cr# [100 × Cr/(Cr + Al) atomic ratio] diagram (after Khedr and Arai, 2017).

Al_2O_3 of 1.29–1.81 wt%, and Cr_2O_3 of 0.25–0.72 wt%. TiO_2 contents of the relict orthopyroxene are extremely low, being lower than the detection limit of the EPMA (< 0.04 wt%; Appendix 1c). In comparison, orthopyroxene inclusions in the Cr-spinel have relatively high Mg# (92–93) and Cr_2O_3 contents (0.79–1.08 wt%) but low Al_2O_3 contents (0.19–0.64 wt%), suggesting that they might be effected by subsolidus re-equilibration with the host Cr-spinel.

Clinopyroxene in the mantle rock samples is dominant by diopside ($En_{48–52}$ $Fs_{2–4}$ $Wo_{44–49}$; Supplementary data 1d). These clinopyroxene grains have similar Mg# [100 × Mg/(Mg + Fe_{tot}) atomic ratio; 94–96] and their TiO_2 contents are almost below the detection limit (Fig. 9d). The interstitial clinopyroxene in serpentinized harzburgite is characterized by low contents of Al_2O_3 (0.74–1.58 wt%), Cr_2O_3 (0.20–0.74 wt%), and Na_2O (0.03–0.11 wt%; Appendix 1d). A positive correlation between Al_2O_3 and Cr_2O_3 was observed in these interstitial clinopyroxene grains, and their Na_2O contents are almost constant with decreasing Mg# (not shown here). Such characteristics suggest that the interstitial clinopyroxene in serpentinized harzburgite might represent the secondary clinopyroxene trapped during melt percolation (Seyler et al., 2007; Uysal et al., 2015). In comparison, clinopyroxene inclusions within the Cr-spinel have relatively low Al_2O_3 contents (0.23–0.92 wt %) but high Cr_2O_3 (0.89–1.74 wt%) and Na_2O contents (0.03–0.28 wt%; Supplementary data 1d). The negative correlation between Na_2O and Mg# in these clinopyroxene inclusions suggests that they might be captured as residues. On the other hand, clinopyroxene in the mafic rock samples is classified as augite ($En_{41–54}$ $Fs_{10–27}$ $Wo_{27–42}$; Supplementary data 1d). Clinopyroxene in gabbro is variable in Mg#, ranging from 62 to 84. Their TiO_2, Al_2O_3, and Cr_2O_3 contents are 0.23–0.61 wt%, 1.45–3.00 wt%, and ≤ 0.68 wt%, respectively. Clinopyroxene phenocrysts in massive basalt have Mg# of 81–85, TiO_2 of 0.22–0.47 wt%, and Cr_2O_3 of 0.47–0.82 wt%, which display a continuously compositional trend with the clinopyroxene in gabbro (Fig. 9d). However, the compositions of clinopyroxene phenocrysts in the pillow basalt differ from this trend. They are characterized by relatively low Mg# (73–80) and high TiO_2 contents (1.00–1.31 wt%; Fig. 9d). Al_2O_3 and Cr_2O_3 contents of these phenocrysts range from 2.20 to 3.07 wt% and from nil to 0.71 wt%, respectively (Supplementary data 1d).

Amphibole included in the Cr-spinel of serpentinite I and serpentinized harzburgite belongs to magnesiohornblende (Fig. 9e), while that in the Cr-spinel of serpentinite II and serpentinite III belongs to pargasite (Fig. 9f). Compared to the magnesiohornblende inclusions (MgO = 20.73–21.68 wt%, Al_2O_3 = 6.09–6.92 wt%, Cr_2O_3 = 2.05–2.79 wt%, TiO_2 ≤ 0.13 wt%, Na_2O = 1.17–1.46 wt%), the pargasite inclusions generally contain lower MgO contents (18.54–20.14 wt%) but higher Al_2O_3 (11.40–13.76 wt%), Cr_2O_3 (2.62–3.44 wt%), TiO_2 (≤ 0.55 wt%), and Na_2O contents (3.18–3.61 wt%; Supplementary data 1e).

4.3. Geochemistry

Whole rock geochemical data of the studied rock samples are listed in Table 1. The studied rock samples have LOI values ranging between 1.43 and 15.57 wt%. In order to reduce the effect of variable element dilution caused by alteration, all major elements were normalized on a volatile-free basis.

The sole serpentinite I sample we analyzed is characterized by relatively low MgO contents (~ 30.74 wt%) and high SiO_2 (~ 53.98 wt%), CaO (~ 0.56 wt%), and Al_2O_3 contents (~ 3.68 wt%; Table 1). Its Ni, Cr, and V concentrations are ~ 2596, ~ 2446, and ~ 32 ppm, respectively. Chondrite-normalized REE (Fig. 10a) and primitive mantle-normalized multi-element diagrams (Fig. 10b) show that serpentinite I is enriched in light REE and large ion lithophile elements (LILE) relative to heavy REE and high field strength elements (HFSE), respectively. Overall, the concentrations of incompatible trace elements in serpentinite I are higher than those in the chondrite and the primitive mantle. Such high contents of SiO_2 and incompatible trace elements are consistent with the presence of talc (Fig. 4a), tremolite (Fig. 4b), and zircon in serpentinite I, which might result from an external-element addition during metamorphism (Khedr and Arai, 2012; Qiu and Zhu, 2018).

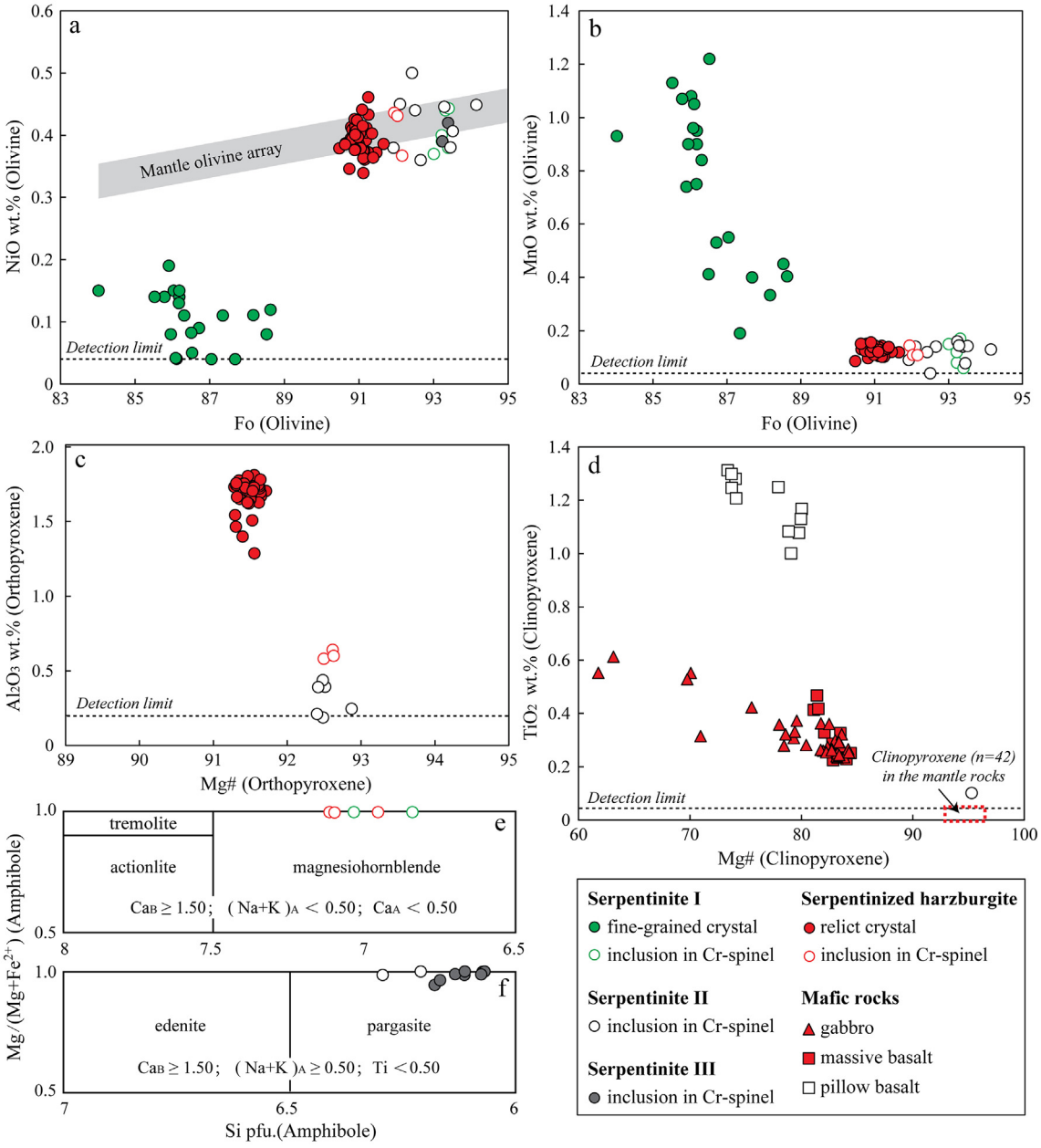

Fig. 9. Compositional variations of olivine, orthopyroxene, clinopyroxene, and amphibole in the studied rock samples. (a) NiO (wt%) and (b) MnO (wt%) vs. Fo [100 × Mg/(Mg + Fe_{tot}) atomic ratio] diagrams for olivine. The mantle olivine array is from Takahashi et al. (1987). (c) Al_2O_3 (wt%) vs. Mg# [100 × Mg/(Mg + Fe_{tot}) atomic ratio] diagram for orthopyroxene. (d) TiO_2 (wt%) vs. Mg# diagram for clinopyroxene. (e, f) Classification diagrams for amphibole (after Leake et al., 1997).

Serpentinite II samples (except samples F10 and F11) display broadly similar major element compositions (Table 1), with SiO_2 contents ranging from 40.26 to 42.75 wt%. They are extremely poor in Ti and other fertility indicators (Al, Ca, Na; Table 1). Furthermore, the concentrations of Ni, Cr, and V are 3145–4263 ppm, 2568–3525 ppm, and 12–34 ppm, respectively. Total REE abundances are depleted in serpentinite II compared to the chondrite (Fig. 10a). They generally display a pattern of depletion from light REE to middle REE that ends with a slightly enrichment of heavy REE (Fig. 10a). Systematic positive Eu anomalies ($Eu/Eu^* = 1.79–2.64$) could be observed in these samples (Fig. 10a). They exhibit enrichments in LILE relative to HFSE on the primitive mantle-normalized multi-element diagram (Fig. 10b). Whole-rock geochemistry of samples F10 and F11 represents a hybrid composition between serpentinite II and serpentinite III because these two samples contain abundant lenses of serpentinite III (Figs. 3c, 6a). TiO_2 (0.05–0.10 wt%; Table 1) and Al_2O_3 contents (0.08–0.26 wt%) of samples F10 and F11 are relatively high. They also have higher concentrations of incompatible trace elements than other serpentinite II samples (Figs. 10a-b).

Serpentinized harzburgite has higher contents of SiO_2 (43.11–44.19 wt%) and V (22–45 ppm), and lower contents of Ni (2088–2531 ppm) and Cr (2480–3071 ppm) than serpentinite II. The total REE abundances of serpentinized harzburgite are extremely poor, being below 0.2 time chondritic values. Additionally, it exhibits a typically U-shaped pattern on the chondrite-normalized REE diagram (Fig. 10a). Elements, such as U, Ta, Zr, and Hf, give a spiked pattern on the primitive mantle-normalized multi-element diagram (Fig. 10b).

Gabbro, with Mg# [molar 100 × MgO/(MgO + FeO_{tot})] varying from 56 to 64 (Table 1) has relatively low contents of SiO_2 (49.37–50.59 wt%) and TiO_2 (0.83–1.04 wt%), and high contents of CaO (10.42–11.79 wt%). Ni, Cr, and V concentrations of gabbro are 48–71, 208–370, and 274–311 ppm, respectively. Compared to the gabbroic samples, massive basalt generally contains higher SiO_2 (51.33–51.59 wt%), TiO_2 (1.02–1.05 wt %), and V (313–319 ppm) concentrations but lower CaO (8.09–8.75 wt

Table 1
Whole-rock major (determined by XRF) and trace (determined by XRF and ICP-MS) elements compositions of the studied rock samples in the north Tianshan ophiolite.

Rock type	Serpentinite I		Serpentinite II							
Sample no.	F1	F2	F7	F8	F9	F10	F11	F12	F13	F14
Major elements determined by XRF (wt%)										
SiO_2	53.98		41.83	40.84	42.08	42.43	41.29	42.04	40.24	42.25
TiO_2	0.19		–	0.01	–	0.05	0.10	–	–	–
Al_2O_3	3.68		–	–	–	0.08	0.26	–	–	–
MgO	30.74		47.50	48.57	47.48	46.19	46.73	47.23	48.79	46.86
MnO	0.19		0.12	0.15	0.13	0.10	0.11	0.11	0.18	0.11
TFe_2O_3	9.90		10.48	10.38	10.26	11.10	11.48	10.58	10.46	10.73
CaO	0.56		–	–	–	–	–	–	0.24	–
Na_2O	0.37		–	–	–	–	–	–	–	–
K_2O	0.37		–	–	–	–	–	–	–	–
P_2O_5	0.02		–	–	–	–	–	–	–	–
LOI	8.02		14.59	15.00	14.48	14.13	14.56	14.41	15.57	14.36
Mg#	86		90	90	90	89	89	90	90	90
Trace elements determined by XRF (ppm)										
Ni μ/g	2596		3393	3958	3468	3320	3257	3837	3803	2845
Cr μ/g	2446		3365	2921	2920	3598	3478	3525	2958	2568
V μ/g	32		18	26	29	9	19	12	25	34
Trace elements determined by solution ICP-MS (ppm)										
Rb	10.32	10.20	–	0.025	–	0.343	0.390	0.228	–	0.072
Ba	149.3	152.9	1.712	0.914	0.572	0.997	2.227	2.427	0.984	2.151
Th	0.805	0.807	0.010	0.012	0.008	0.083	0.081	0.017	0.007	0.034
U	0.285	0.300	0.028	0.012	0.015	0.041	0.026	0.034	0.011	0.026
Ta	0.420	0.240	0.010	0.012	0.013	0.190	0.200	0.015	0.028	0.054
Nb	1.613	1.346	0.081	0.102	0.094	0.955	1.796	0.114	0.120	0.192
Zr	41.64	41.08	0.703	0.773	0.534	3.620	8.500	0.608	0.481	0.498
Hf	1.214	1.194	0.019	0.014	0.015	0.107	0.256	0.017	0.020	0.017
Y	6.177	6.118	0.100	0.046	0.094	0.734	0.970	0.080	0.112	0.053
La	4.130	4.066	0.280	0.158	0.191	0.488	0.488	0.231	0.108	0.097
Ce	9.227	9.119	0.584	0.346	0.394	1.010	1.091	0.432	0.176	0.191
Pr	1.064	1.236	0.085	0.043	0.051	0.124	0.146	0.059	0.029	0.024
Nd	4.603	5.339	0.300	0.190	0.220	0.533	0.747	0.233	0.138	0.110
Sm	0.978	0.986	0.049	0.034	0.035	0.102	0.151	0.042	0.031	0.028
Eu	0.297	0.298	0.031	0.022	0.017	0.028	0.023	0.017	0.014	0.014
Gd	1.023	1.031	0.040	0.013	0.030	0.119	0.178	0.023	0.025	0.021
Tb	0.170	0.172	0.004	0.002	0.004	0.021	0.032	0.003	0.004	0.003
Dy	1.024	1.055	0.025	0.009	0.019	0.132	0.189	0.017	0.023	0.013
Ho	0.219	0.219	0.004	0.002	0.004	0.028	0.038	0.003	0.005	0.002
Er	0.638	0.641	0.011	0.005	0.011	0.078	0.111	0.008	0.014	0.007
Tm	0.101	0.101	0.002	0.001	0.002	0.011	0.017	0.001	0.002	0.001
Yb	0.663	0.662	0.013	0.008	0.013	0.072	0.114	0.010	0.015	0.008
Lu	0.107	0.107	0.003	0.001	0.002	0.012	0.019	0.002	0.003	0.001
δEu	0.90	0.90	2.06	2.60	1.59	0.79	0.43	1.53	1.52	1.71
$(La/Yb)_N$	4.47	4.41	15.30	14.96	10.65	4.85	3.06	16.62	5.16	8.19
$(Dy/Yb)_N$	1.03	1.07	1.27	0.83	0.98	1.23	1.10	1.12	1.02	0.99
Ba/La	36.15	37.60	6.12	5.78	3.00	2.04	4.56	10.52	9.07	22.17
Ba/Th	185	190	169	77	74	12	27	142	144	64
Th/Nd	0.17	0.15	0.03	0.06	0.04	0.15	0.11	0.07	0.05	0.31

Rock type	Serpentinite II				Serpentinized harzburgite				
Sample no.	F15	F16	F17	F18	F27	16F83	16F85	16F86	16F87
Major elements determined by XRF (wt%)									
SiO_2	40.35	42.55	42.72	42.26	43.85	43.57	43.65	44.19	43.11
TiO_2	–	–	–	–	–	–	–	–	–
Al_2O_3	–	–	–	–	–	–	–	–	–
MgO	47.49	44.50	45.37	46.91	45.49	45.77	45.61	45.22	46.66
MnO	0.11	0.10	0.11	0.09	0.05	0.11	0.15	0.14	0.16
TFe_2O_3	12.00	12.80	11.75	10.68	10.55	10.54	10.59	10.12	10.07
CaO	–	–	–	–	–	–	–	–	–
Na_2O	–	–	–	–	–	–	–	–	–
K_2O	–	–	–	–	–	–	–	–	–
P_2O_5	–	–	–	–	–	–	–	–	–
LOI	14.68	14.06	14.84	14.24	14.81	14.59	14.29	11.53	14.27
Mg#	89	87	88	90	90	90	90	90	90
Trace elements determined by XRF (ppm)									
Ni μ/g	4263	4225	4071	3355	2531	2231	2319	2088	2358
Cr μ/g	2872	3226	3181	3426	3071	2480	2774	2791	2962
V μ/g	29	22	14	14	22	45	42	40	28
Trace elements determined by solution ICP-MS (ppm)									
Rb	0.125	0.113	–	–	0.059	0.037	0.242	0.185	
Ba	3.017	2.161	0.898	1.328	2.243	1.909	2.254	2.769	

Table 1 (*continued*)

Rock type	Serpentinite II				Serpentinized harzburgite				
Sample no.	F15	F16	F17	F18	F27	16F83	16F85	16F86	16F87
Th	0.009	0.006	0.007	0.010	0.004	–	–	–	
U	0.038	0.018	0.022	0.031	0.028	0.028	0.026	0.021	
Ta	0.022	0.018	0.009	0.009	0.010	–	0.011	–	
Nb	0.075	0.050	0.042	0.087	0.050	–	–	–	
Zr	0.692	0.477	0.500	0.653	0.434	0.254	0.604	0.623	
Hf	0.018	0.012	0.015	0.018	0.009	0.000	0.011	0.014	
Y	0.054	0.053	0.133	0.102	0.018	0.023	0.059	0.031	
La	0.068	0.081	0.063	0.099	0.012	0.026	0.049	0.029	
Ce	0.133	0.112	0.100	0.182	0.025	0.043	0.094	0.054	
Pr	0.018	0.013	0.015	0.031	0.004	0.006	0.010	0.006	
Nd	0.096	0.068	0.066	0.129	0.015	0.021	0.040	0.020	
Sm	0.025	0.023	0.020	0.032	0.003	0.003	0.010	0.004	
Eu	0.017	0.017	0.012	0.021	0.001	0.001	0.002	0.001	
Gd	0.026	0.014	0.016	0.016	0.003	0.003	0.007	0.004	
Tb	0.003	0.002	0.003	0.003	0.000	0.000	0.001	0.001	
Dy	0.015	0.010	0.021	0.020	0.003	0.003	0.008	0.005	
Ho	0.003	0.002	0.005	0.004	0.001	0.001	0.002	0.001	
Er	0.007	0.007	0.010	0.011	0.003	0.004	0.008	0.005	
Tm	0.001	0.001	0.002	0.002	0.001	0.001	0.002	0.001	
Yb	0.008	0.008	0.010	0.012	0.009	0.010	0.019	0.014	
Lu	0.001	0.002	0.001	0.002	0.002	0.002	0.003	0.003	
δEu	2.00	2.64	1.92	2.44	0.90	0.84	0.80	0.90	
$(La/Yb)_N$	6.10	7.55	4.54	5.79	0.92	1.85	1.83	1.49	
$(Dy/Yb)_N$	1.30	0.87	1.40	1.08	0.22	0.20	0.28	0.24	
Ba/La	44.46	26.65	14.21	13.47	188.13	74.17	46.40	95.49	
Ba/Th	324	350	122	138	506	–	–	–	
Th/Nd	0.10	0.09	0.11	0.07	0.30	–	–	–	

Rock type	Gabbro				Massive basalt		Pillow basalt			
Sample no.	16F90	16F91	16F92	16F98	16F95	16F96	F28	F29	16F88	16F89
Major elements determined by XRF (wt%)										
SiO_2	50.48	50.59	50.00	49.37	51.33	51.59	59.33	52.15	49.76	52.18
TiO_2	1.04	0.83	0.93	0.95	1.02	1.02	3.39	3.56	3.56	3.83
Al_2O_3	13.90	14.44	14.51	14.88	13.92	13.72	13.25	13.81	14.92	15.05
MgO	8.17	9.40	8.37	8.51	7.88	7.19	2.99	3.89	3.92	3.77
MnO	0.21	0.20	0.21	0.21	0.23	0.19	0.12	0.12	0.12	0.12
TFe_2O_3	12.59	10.53	12.31	12.15	13.41	12.79	8.86	12.59	12.64	11.25
CaO	10.52	11.12	11.79	10.42	8.09	8.75	4.89	7.79	8.97	6.69
Na_2O	2.83	2.62	1.76	2.35	4.00	4.15	5.63	4.70	3.90	4.33
K_2O	0.20	0.21	0.07	1.08	0.05	0.52	0.68	0.55	1.61	2.00
P_2O_5	0.07	0.04	0.06	0.07	0.08	0.08	0.86	0.84	0.59	0.78
LOI	2.48	3.08	1.43	2.71	2.05	2.20	2.06	2.74	2.03	2.07
Mg#	56	64	57	58	54	53	40	38	38	40
Trace elements determined by XRF (ppm)										
Ni	48	58	53	71	50	52	–	–	–	–
Cr	208	370	292	304	235	241	8	23	48	6
V	311	274	295	296	289	313	166	218	164	178
Trace elements determined by solution ICP-MS (ppm)										
Rb	3.21	4.14		22.3	5.60	8.90	14.3		43.3	50.2
Ba	105	84.7		125	94	127	302		263	323
Th	0.26	0.20		0.22	0.22	0.24	6.08		5.10	6.68
U	0.09	0.05		0.06	0.081	0.11	2.35		1.00	1.57
Ta	0.17	0.12		0.14	0.19	0.18	1.51		2.28	2.47
Nb	2.74	1.92		2.17	2.58	2.22	33.9		37.4	43.5
Zr	53.4	42.4		48.8	45.5	53.1	328		313	392
Hf	1.58	1.25		1.44	1.37	1.56	8.40		7.78	9.68
Y	19.7	16.0		18.4	16.5	20.1	44.9		37.7	49.8
La	2.98	2.41		2.74	2.15	2.84	45.9		37.4	46.6
Ce	7.97	6.00		6.92	6.54	7.53	90.4		76.6	97.8
Pr	1.25	0.99		1.15	1.04	1.23	12.1		10.6	13.5
Nd	6.59	5.17		6.04	5.112	6.50	52.6		45.4	59.6
Sm	2.29	1.79		2.07	1.85	2.26	11.4		10.3	13.1
Eu	0.88	0.68		0.83	0.71	0.85	3.19		3.13	3.92
Gd	2.70	2.14		2.46	2.35	2.68	10.7		9.46	12.1
Tb	0.58	0.45		0.53	0.44	0.57	1.81		1.60	2.06
Dy	3.81	3.01		3.53	3.05	3.83	9.92		8.68	11.2
Ho	0.83	0.66		0.76	0.68	0.83	1.86		1.61	2.10
Er	2.41	1.91		2.23	1.87	2.45	4.84		4.17	5.39
Tm	0.37	0.29		0.34	0.27	0.37	0.66		0.56	0.74
Yb	2.38	1.87		2.19	1.81	2.37	3.98		3.36	4.39
Lu	0.36	0.28		0.33	0.27	0.36	0.56		0.48	0.62

(*continued on next page*)

Table 1 (*continued*)

Rock type	Gabbro				Massive basalt		Pillow basalt			
Sample no.	16F90	16F91	16F92	16F98	16F95	16F96	F28	F29	16F88	16F89
δEu	1.08	1.05		1.13	1.04	1.05	0.87		0.95	0.94
$(La/Yb)_N$	0.90	0.92		0.90	0.85	0.86	8.27		7.98	7.62
$(Dy/Yb)_N$	1.07	1.07		1.08	1.13	1.08	1.67		1.73	1.71
Ba/La	35.20	35.15		45.53	43.58	44.56	6.58		7.04	6.93
Ba/Th	410	425		564	425	536	50		52	48
Th/Nd	0.04	0.04		0.04	0.04	0.04	0.12		0.11	0.11

Mg# = [molar 100 × MgO/(MgO + FeO_{tot})]; —: Below detection limited.

%), Ni (50–52 ppm), and Cr (235–241 ppm) concentrations. In general, most major elements in gabbro and massive basalt show nearly linear variations with their Mg#. Gabbro and massive basalt exhibit similar chondrite-normalized REE and primitive mantle-normalized multi-element patterns (Fig. 10c–d), which are akin to those of N-MORB. However, they are characterized by flatter REE patterns with $(La/Yb)_N$ values of 0.85–0.92 (Table 1) compared to N-MORB [$(La/Yb)_N = 0.56$]. In addition, they have higher concentrations of Ba, Rb Th, and U than N-MORB. Pillow basalt exhibits distinct compositional trends from massive basalt and gabbro, characterized by high TiO_2 contents (3.39–3.83 wt%; Table 1) and low V concentrations (164–218 ppm). Moreover, it has lowest Mg# (38–40), Ni (~0 ppm), and Cr (<48 ppm) concentrations. Pillow basalt shows a similar trace element signature to OIB (Fig. 10c–d), which is typically enriched in light REE with respect to heavy REE.

5. Discussion

5.1. Petrogenesis of the mantle rocks

The modal abundances of clinopyroxene are useful indicators for tracing the partial melting processes in mantle peridotites (Dai et al., 2011; Uysal et al., 2015) because clinopyroxene is considered as the most rapidly consumed mineral during anhydrous melting of spinel facies lherzolites (Jaques and Green, 1980). The low modal abundance or even the absence of clinopyroxene (< 3 vol%) in the studied serpentinized harzburgites indicates that these rocks underwent high degrees of partial melting. This is supported by their extremely low whole rock concentrations of CaO, Al_2O_3, and TiO_2 (Table 1), which are progressively depleted with an increasing extent of melting (Pearce et al., 1992). The high Fo (90–92; Fig. 9a) of the relict olivine and the low Al_2O_3 contents (1.29–1.81 wt%; Fig. 9c) of the relict orthopyroxene in the serpentinized harzburgites are also consistent with elevated degrees of partial melting (Czertowicz et al., 2016). Although the exact modal mineralogy of other mantle rock samples has been obscured by post-magmatic processes, low CaO, Al_2O_3, and TiO_2 contents (Table 1) in these rocks can reflect their high-degree melting nature.

We chose the whole-rock Ni and Yb concentrations to constrain the degree of partial melting of the studied mantle rocks because the concentrations of Ni and Yb are almost independent of fluid- and melt-related enrichment processes. Yb is incompatible for major mantle phases such as olivine and pyroxene (Green et al., 2000) and consequently its abundance decreases with increasing degree of partial melting, while Ni behaves compatibly during melting (Suhr, 1999) and its concentration increases with the extent of melting. Therefore, Ni/Yb vs. Yb systematics of mantle peridotites is a useful tool for estimating the degree of partial melting (Uysal et al., 2012). A closed-system non-

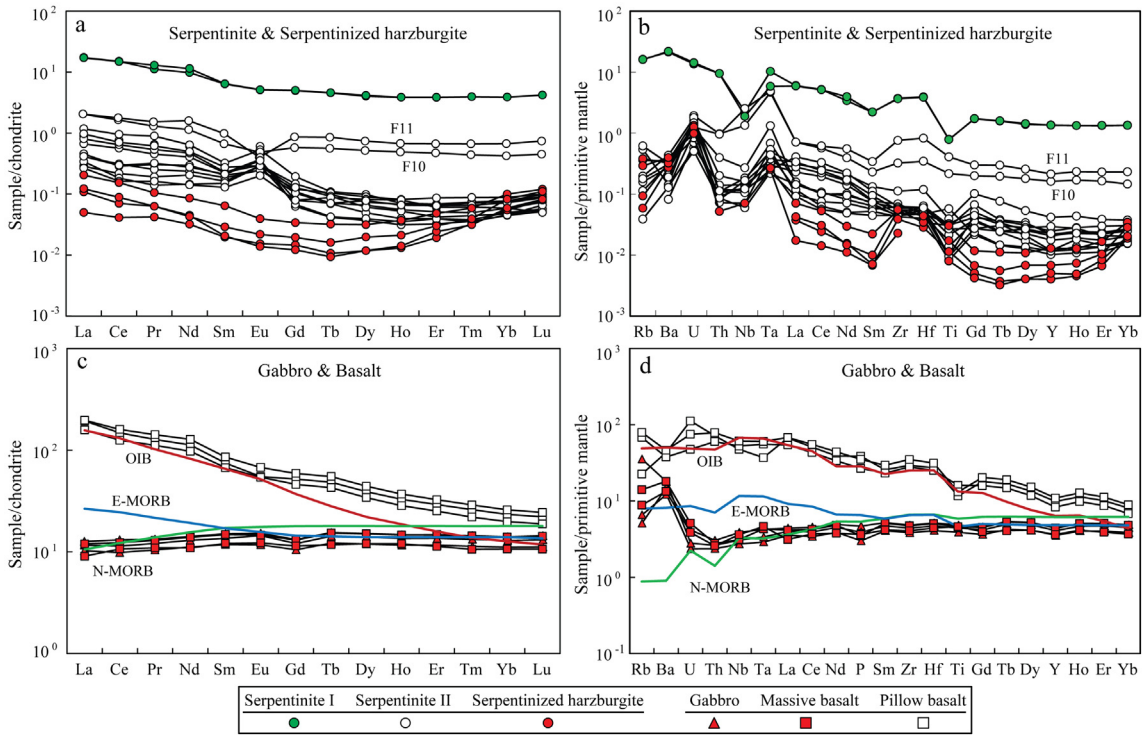

Fig. 10. Chondrite-normalized REE patterns (a, c) and primitive mantle-normalized multi-element diagrams (b, d) of the studied rock samples in the north Tianshan ophiolite. Values of chondrite, primitive mantle, N-MORB, *E*-MORB, and OIB are from Sun and McDonough (1989). F10 and F11 refer to sample F10 and sample F11 respectively, and the whole-rock geochemistry of these two samples represents a hybrid composition between serpentinite II and serpentinite III.

dynamic melting model (Shaw, 2000) was used to calculate the melting trends. The starting composition was assumed to be that of a depleted MORB-type mantle source (DMM; Workman and Hart, 2005). The mantle source modal composition and the eutectic proportions of mantle mineral phases were taken as: $Ol_{0.53(-0.06)} + Opx_{0.27(0.28)} + Cpx_{0.17(0.67)} + Sp_{0.03(0.11)}$ (Kinzler, 1997). Clinopyroxene was exhausted after approximately 25% partial melting, and a new modal composition was calculated for higher degrees of melting, which was: $Ol_{0.73(-0.18)} + Opx_{0.27(0.85)} + Sp_{0.02(0.33)}$. Accordingly, it could be estimated that serpentinized harzburgite experienced 22–27% partial melting from DMM, whereas the other mantle rock samples (except samples F10 and F11) were subjected to higher (26–29%) degrees of melting (Fig. 11a). The Ni and Yb concentrations of samples F10 and F11 correspond to 13–17% melting. The whole-rock compositions of these two samples represent a hybrid composition between serpentinite II and serpentinite III. Thus, serpentinite III should undergo lower degrees of melting than serpentinite II.

However, several lines of evidence suggest that the origin of the studied mantle rocks could not be interpreted by partial melting alone. They also underwent variable melt-rock interaction processes. The first evidence comes from the presence of small interstitial clinopyroxene (Fig. 7a) between the olivine and the orthopyroxene grains in the studied serpentinized harzburgites. Such clinopyroxene has different texture and composition from the residual clinopyroxene (Uysal et al., 2016) and is often considered to be formed during melt percolation through mantle peridotites (Saka et al., 2014). Second, the occurrence of hydrous silicate inclusions, such as magnesiohornblende (Figs. 4h, 7i) and pargasite (Figs. 5e–f, 6f) within the Cr-spinel provides another evidence for the reactions between melts and residual peridotites (Morishita et al., 2011; Tamura et al., 2016). It has been suggested that these inclusions crystallize from the trapped melts produced by melt-rock interactions combined with zone refining effects (Arai et al., 1997). Although the compositions of hydrous silicate inclusions within the Cr-spinel do not directly reflect the parent melt composition which reacted with the host peridotites, the low TiO_2 contents (≤0.55 wt%; Supplementary data 1e) of the studied amphibole inclusions suggest that the mantle rocks were interacted with hydrous TiO_2-poor melts rather than MORB-related melts (Morishita et al., 2011). Third, it has been suggested that the morphology of Cr-spinel is dependent on the genetic processes affecting its host rock (Kapsiotis, 2013; Matsumoto and Arai, 2001). For example, the nature of the melting residue can be inferred from the anhedral shape of Cr-spinel, whereas the euhedral Cr-spinel is more likely to crystallize from percolating melts. Therefore, the presence of euhedral Cr-spinel grains (Figs. 4f, 5d–f, 6d–f, 7d) in the studied mantle rocks suggests that they have been modified by the percolating melt during melt-rock interactions. This is consistent with the compositions of Cr-spinel, which show the evidence of interaction of melts with different compositions. Cr-spinel cores in serpentinite III have moderate Cr# (54–68), and exhibit a wide variation in TiO_2 contents (≤ 0.41 wt%; Supplementary data 1a). Titanium is incompatible during partial melting and its content is expected to decrease as the melting degree increases (Kinzler and Grove, 1992; Pearce et al., 2000). Thus, the enrichment of TiO_2 in the Cr-spinel cores could not be explained by partial melting. Instead, interaction between a harzburgitic residue and a melt with island arc tholeiitic composition might be the best explanation for such high contents of TiO_2 in these Cr-spinel cores (Fig. 11b). On the other hand, Cr-spinel cores (Cr# > 70) in serpentinite I and serpentinite II have relatively low but appreciable TiO_2 contents (≤ 0.15 wt%; Supplementary data 1a). Such Cr-spinel was most likely produced by interaction between a highly depleted mantle and a melt which is poor in Ti and rich in Cr (i.e., boninitic melt; Fig. 11b).

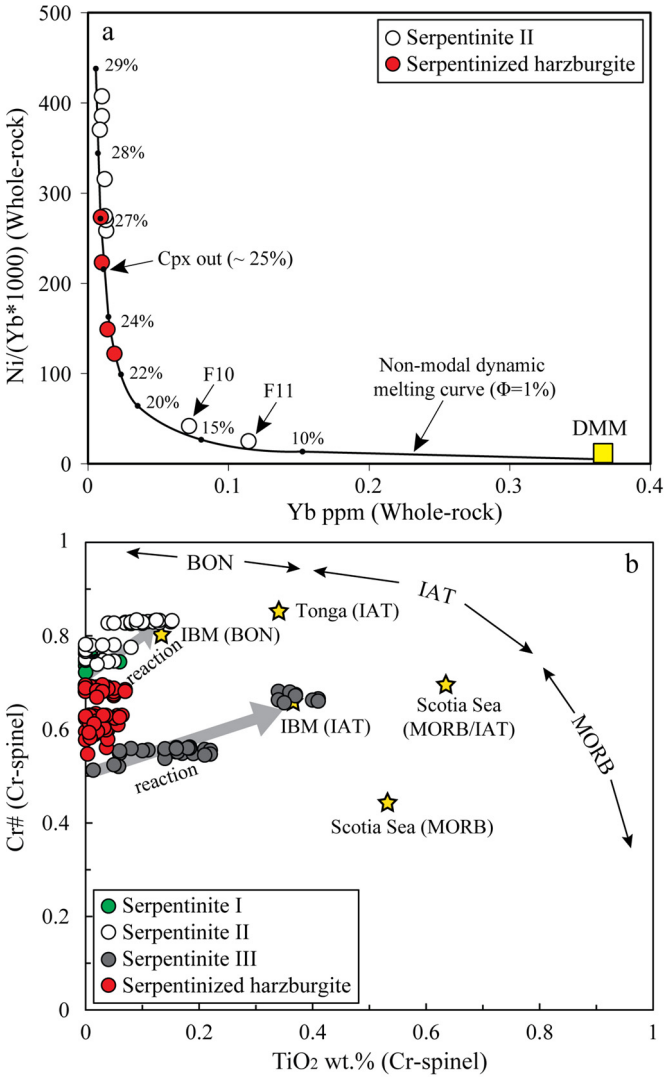

Fig. 11. (a) Ni/Yb vs. Yb diagram for the mantle rock samples, on which closed-system non-modal dynamic melting model is shown. Starting composition for the melting model is depleted MOR mantle (DMM, Workman and Hart, 2005) with $Ol_{0.53(-0.06)} + Opx_{0.27(0.28)} + Cpx_{0.17(0.67)} + Sp_{0.03(0.11)}$ mineralogy (Kinzler, 1997). Partition coefficients are from Uysal et al. (2012). F10 and F11 refer to sample F10 and sample F11, respectively. (b) Plot of Cr# vs. TiO_2 (wt%) for primary Cr-spinel cores in the mantle rock samples, on which melt-peridotite interaction trends are shown. Fields of IBM (BON), IBM (IAT), Tonga (IAT), Scotia Sea (MORB/IAT) and Scotia Sea (MORB) are from Pearce et al. (2000). Abbreviations: IBM, Izu-Bonin-Mariana; BON, boninite; IAT, island arc tholeiite; MORB, mid-ocean ridge basalt.

5.2. The origin of the mafic rocks

Incompatible element ratios with a common denominator (Yb) can minimize the effects of partial melting and fractional crystallization (and/or cumulation), and thus can be used to trace magma sources (Pearce and Peate, 1995). We used the Zr/Yb vs. Nb/Yb diagram to show the depletion of mantle during partial melting (Condie, 2005). Fig. 12a shows that all the studied mafic rocks fall within the MORB-OIB array, with pillow basalt closing to OIB end-member and others closing to N-MORB, suggesting that the studied pillow basalt was originated from an enriched mantle, whereas gabbro and massive basalt were derived from a depleted MORB mantle. This is further supported by the OIB-like REE patterns of the pillow basalt and the N-MORB-like REE patterns of gabbro and massive basalt (Fig. 10c).

TiO_2/Yb vs. Nb/Yb diagram was chosen to highlight the melting depth proxy (Pearce, 2008). In Fig. 12b, pillow basalt plots into the OIB field while gabbro and massive basalt fall in the MORB field, suggesting that the pillow basalt was generated by partial melting within garnet stability zone, whereas gabbro and massive basalt were produced by melting of a spinel-facies mantle source. This is consistent

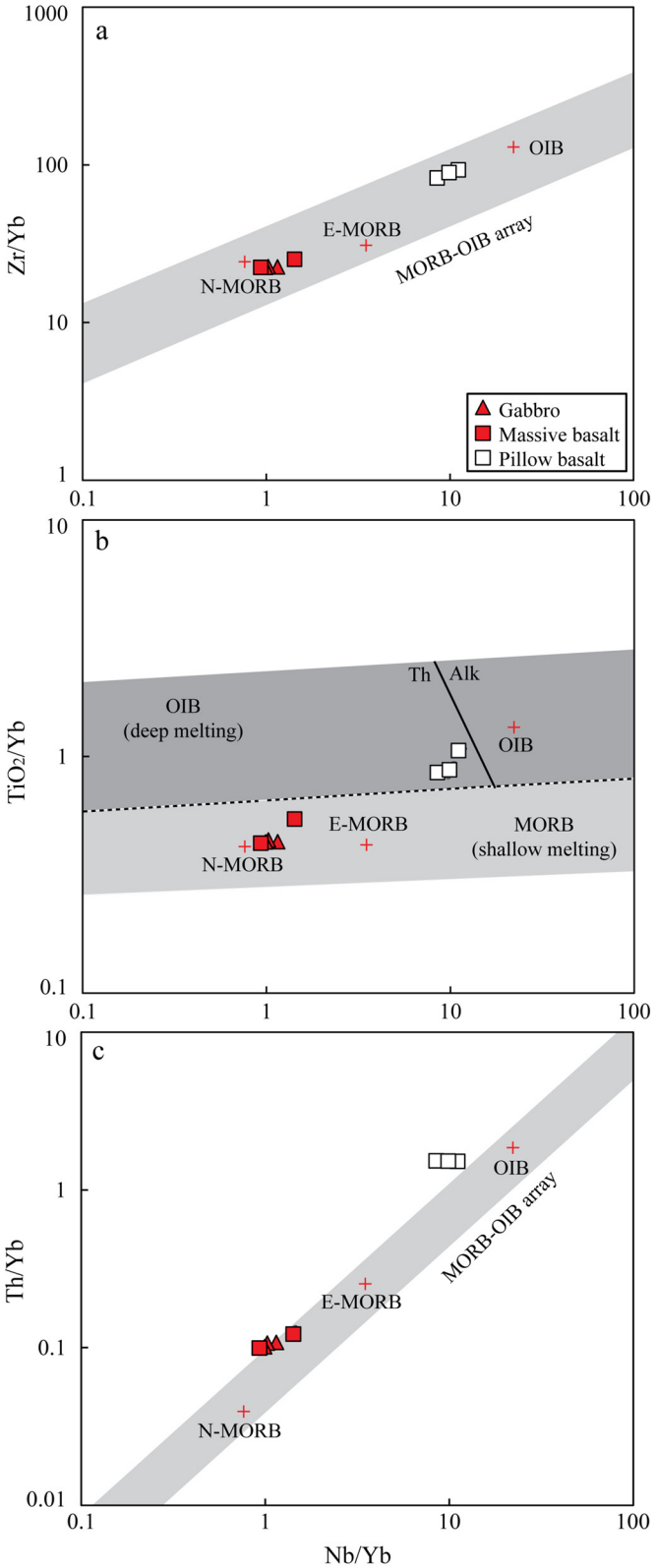

Fig. 12. (a) Zr/Yb, (b) TiO_2/Yb, and (c) Th/Yb vs. Nb/Yb diagrams for the mafic rock samples. Shallow and deep melting fields in plane b and the MORB-OIB array in plane c are based on Peace (2008).

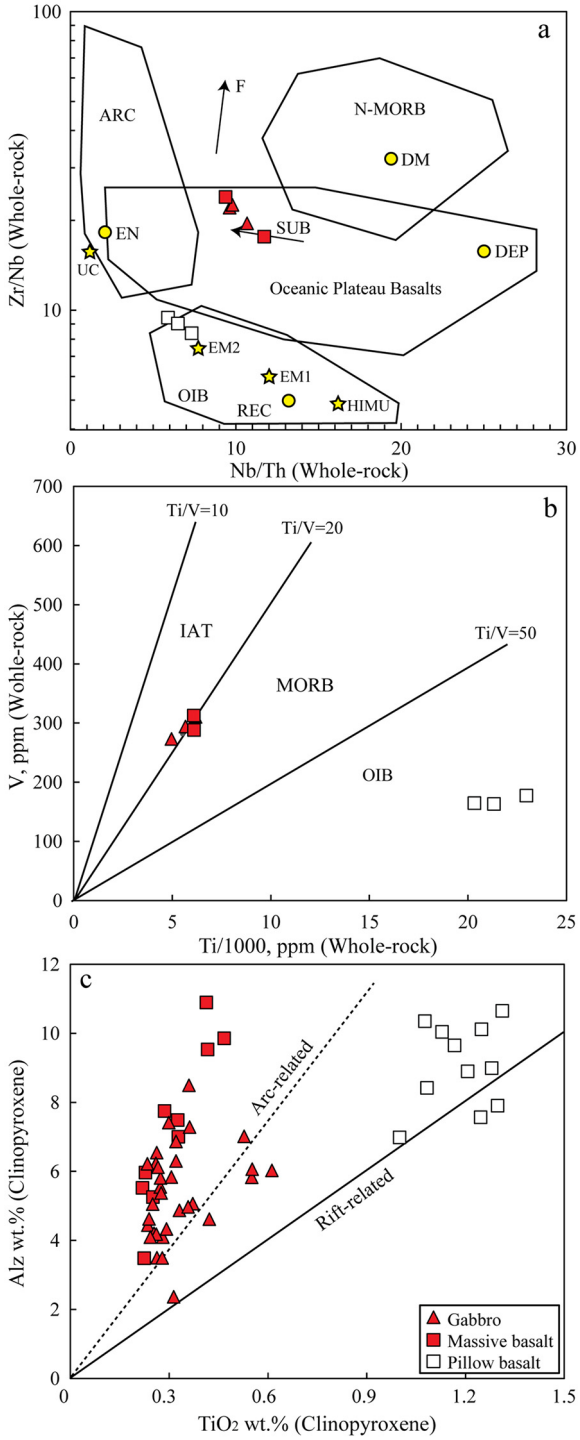

Fig. 13. (a) Zr/Nb vs. Nb/Th diagram (after Condie et al., 2005) for the mafic rock samples. Arrows indicate effects of batch melting (F) and subduction (SUB). Abbreviations: UC, upper continental crust; DM, shallow depleted mantle; HIMU, high μ (U/Pb) source; EM1 and EM2, enriched mantle sources; ARC, arc related basalts; N-MORB, normal mid-ocean ridge basalt; OIB, oceanic island basalt; DEP, deep depleted mantle; EN, enriched component; REC, recycled component. (b) V (ppm) vs. Ti/1000 (ppm) diagram (after Shervais, 1982) for the mafic rock samples. Abbreviations: IAT, island arc tholeiite; MORB, mid-ocean ridge basalt; OIB, ocean island basalt. (c) Correlations of Alz (percentage of tetrahedral sites occupied by Al) vs. TiO_2 (wt%) of clinopyroxene in the mafic rock samples. Reference trends in arc- and rift-related are based on Loucks (1990).

with the higher $(Dy/Yb)_N$ ratios of pillow basalt (1.70–1.72; Table 1) than those of gabbro and massive basalt (1.07–1.13; Table 1).

On the Th/Yb vs. Nb/Yb diagram, the studied mafic rocks fall within or slightly above the MORB-OIB array (Fig. 12c), indicating that they were slightly affected by crustal addition (Pearce, 2014). There are three main crustal inputs at the present day: crustal contamination during magma ascent, addition of slab-derived fluids and/or melts to the overlying mantle wedge through dehydration and/or melting processes,

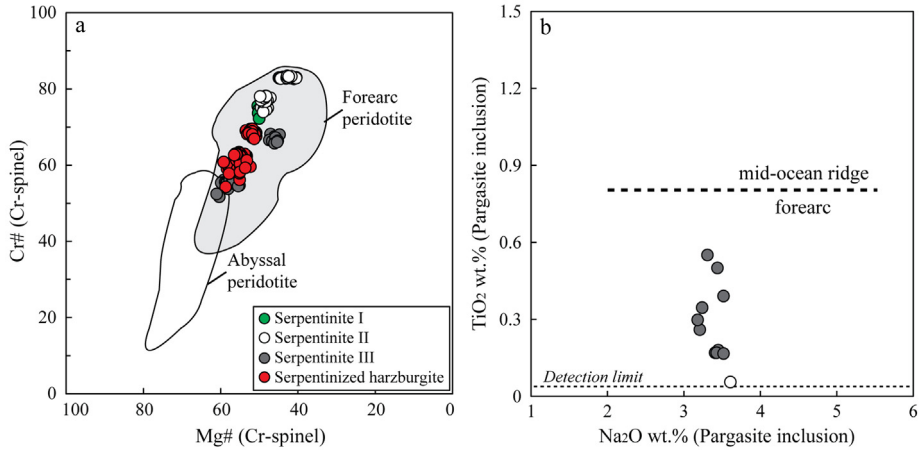

Fig. 14. (a) Cr# vs. Mg# diagram for primary Cr-spinel cores in the mantle rock samples. The abyssal peridotite field is from Dick and Bullen (1984), and the forearc peridotite field is from Ishii et al. (1992) and Parkinson and Pearce (1998). (b) Na_2O (wt%) vs. TiO_2 (wt%) diagram for the pargasite inclusions within the Cr-spinel. The boundary between mid-ocean ridge and forearc is based on Tamura et al. (2016).

and incorporation of crustal materials (e.g., chemically modified slab components and lower continental crust) in the mantle via subduction or delamination. The studied pillow basalt has slightly higher Th/Yb ratios than the Hawaiian tholeiites, but lower than OIB forming in the continental setting or subduction zone at a given Nb/Yb ratio (Pearce, 2008). On the Zr/Nb vs. Nb/Th diagram, the pillow basalt falls close to the enriched mantle 2 (EM2-type mantle) end member of the recycled component field (Fig. 13a). Combined with the low trace element ratios that are sensitive to additions of slab-derived components (e.g., Ba/La = 6.6–7.0, Ba/Th = 48–52, and Th/Nd = 0.11–0.12; Table 1), we suggest that the mantle source of the pillow basalt was affected by the EM2-type mantle components rather than by slab-derived fluids and/or melts. By contrast, massive basalt and gabbro have much higher Ba/La (35–46) and Ba/Th (410–564) but similar Th/Nd ratios (~ 0.03; Table 1) compared to N-MORB (Ba/La = 2.5, Ba/Th = 2.7, Th/Nd = 0.02; Sun and McDonough, 1989), indicating that their mantle source was modified by slab-derived fluids. Such subduction signatures are also revealed by their low Ti/V ratios (~ 20; Fig. 13b), which are typical of island arc tholeiite as well as their clinopyroxene compositions, which plot in the arc-related field on Alz (Alz = percentage of tetrahedral sites occupied by Al) vs. TiO_2 diagram (Fig. 13c).

The OIB-like rocks may be derived from an OIB reservoir through a mantle plume (White, 2010) or generated by decompression melting of an enriched metasomatized mantle in mid-ocean ridges (Khogenkumar et al., 2016). The OIB can also be found in some arc-related settings, such as slab rolling back inducing interactions between asthenospheric and lithospheric mantle (Ferrari et al., 2001; Tang et al., 2012), melting of the mantle wedge metasomatized by subducted alkaline basalts (i.e., old seamounts; Yang et al., 2015), and upwelling of an enriched asthenosphere through a slab window during ridge subduction (Cole and Stewart, 2009). If the OIB formed in mid-ocean ridges, enriched basalts such as *E*-MORB should also be found. However, there are no E-MORB documented in this region (Yang et al., 2018), suggesting that the OIB-like pillow basalt in the north Tianshan ophiolite was not produced in a mid-ocean ridge setting. If the OIB was derived from the overlying lithospheric mantle interacting with ascending asthenosphere or subducted alkaline basalts in arc-related settings, it would show geochemical features of both intra-plate and island arc magmatic rocks (Ferrari et al., 2001; Tang et al., 2012; Zhu et al., 2001). As mentioned above, the studied pillow basalt shows no arc-related signatures, suggesting that it did not form in such environments. Due to the absence of available geochronological data, it is difficult to determine whether the studied OIB-like pillow basalt was derived from a mantle plume or a slab window related to ridge subduction. However, based on the lack of other key features attributed to ridge subduction, such as adakitic magmatism and high-temperature metamorphism (Cole and Stewart, 2009; Guo et al., 2013) in the NTAC, we prefer that the studied pillow basalt represents the fragment of seamounts derived from the mantle plume.

5.3. Tectonic implications

Ophiolites formed in a forearc setting (e.g., Izu-Bonin-Mariana forearc) are characterized by systematic variations in lava compositions, from initially MORB-like through island arc tholeiitic to boninitic (Saccani et al., 2017; Stern et al., 2012). The occurrence of highly refractory mantle rocks is also an important and distinctive feature of forearc ophiolites (Abdel-Karim et al., 2016; Marchesi et al., 2016; Morishita et al., 2011). The whole-rock compositions of massive basalt and gabbro in the north Tianshan ophiolite (Table 1) are comparable to those of the Izu-Bonin-Mariana forearc basalt (Reagan et al., 2010). The compositions of Cr-spinel in the samples of serpentinite I, serpentinite II, and serpentinite III record the interactions with island arc tholeiitic and boninitic melts (Fig. 11b), and such related crustal rocks have been documented in the NTAC (Li et al., 2015; Zhao et al., 2007). Combined with the mineral (Supplementary data) and whole-rock (Table 1) compositional data of the mantle rock samples, which are similar to those of forearc peridotites (Fig. 14), we suggest that massive basalt, gabbro, and the mantle rocks in the north Tianshan ophiolite were generated in a forearc setting.

Two mechanisms have been proposed for forearc ophiolites: spontaneous subduction initiation mechanism (Arculus et al., 2015; Whattam and Stern, 2011) and subduction zone decoupling-retreat mechanism (Butler and Beaumont, 2017). The former mechanism is favored in intra-oceanic settings where the subducted lithosphere is old and the upper plate is young and thin, while the latter one is used to explain the forearc ophiolites generated at an active continental margin. Distinguishing between these two mechanisms is that decoupling-retreat mechanism would have a geological record of prior subduction, such as arc magmatism before decoupling, whereas this would be absent in the case of subduction initiation. Early Carboniferous radiolarians found in the chert of the NTAC (Xiao et al., 1992), together with zircon U—Pb ages of 325–344 Ma obtained from plagiogranite and gabbro (Li et al., 2015; Xu et al., 2006) suggest that the north Tianshan ophiolite formed during Early Carboniferous. However, most zircon U—Pb ages and geochemical data of plutonic and volcanic rocks along the north margin of the Yili-central Tianshan terrane (An et al., 2017; Zhang et al., 2008) suggest that southward subduction of the north Tianshan oceanic lithosphere started since Early Devonian. Therefore, we prefer subduction zone decoupling-retreat mechanism to explain

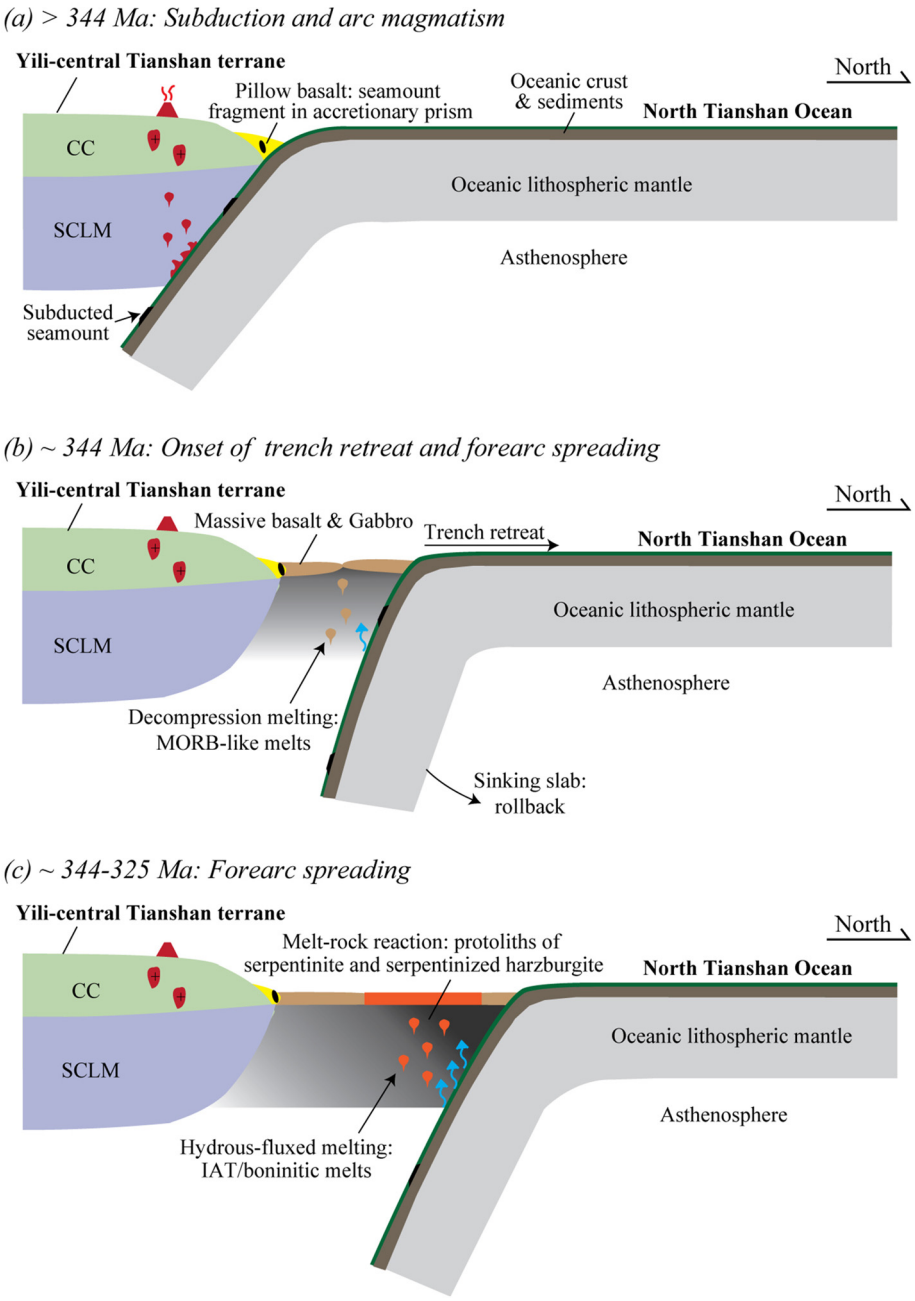

Fig. 15. Schematic cartoons (not to scale) illustrating the formation of the north Tianshan ophiolite. Detailed interpretations are given in the text. Abbreviations: CC, continental crust; SCLM, sub-continental lithospheric mantle; IAT, island arc tholeiite.

the north Tianshan forearc ophiolite (Fig. 15). Southward subduction of the north Tianshan oceanic lithosphere beneath the Yili-central Tianshan terrane since Early Devonian led to the activation of arc magmatism (Fig. 15a). The seamounts, represented by the OIB-like pillow basalt, were likely scraped-off and accreted in the accretionary prism during this stage. Subduction continued until the onset of subduction zone retreat. The northward migration of the trench at Early Carboniferous (~ 344 Ma) triggered the extension of overlying forearc lithosphere, and led to decompression melting of the upwelling asthenosphere, forming massive basalt and gabbro with N-MORB affinities (Fig. 15b). The high ratios of Ba/La and Ba/Th for massive basalt and gabbro indicate that the decompression melting might be enhanced by a flux of slab-derived fluids. Continuous slab sinking and retreat promoted accelerated return flow of the depleted mantle toward the forearc region. Meanwhile, the mantle wedge was progressively metasomatized by fluids/melts releasing from the sinking slab (Fig. 15c). These processes collectively led to high degrees of partial melting, producing island arc tholeiitic to boninitic melts. These melts might interact with refractory mantle residues and formed the mantle rocks (i.e., the protoliths of serpentinite and serpentinized harzburgite) in the north Tianshan ophiolite.

6. Conclusion

The mafic and ultramafic rocks in the north Tianshan ophiolite cropping out along the Duku road mainly consist of pillow basalt, massive basalt, gabbro, serpentinite, and serpentinized harzburgite. Pillow basalt shows an OIB-like geochemical signature, while massive basalt and gabbro display dual features of MORB- and arc-like geochemistry. Serpentinite and serpentinized harzburgite, belonging to the mantle section of the ophiolite, are characterized by highly depleted mineral and whole-rock compositions. Present model based on new petrological

observations and geochemical data suggests that the north Tianshan ophiolite formed in a forearc setting by shifting conditions of melting. Massive basalt and gabbro formed due to decompression melting of upwelling asthenosphere triggered by retreat and rollback of the north Tianshan subducted slab. Refractory harzburgites as well as island arc tholeiitic to boninitic melts formed subsequently as a result of enhanced partial melting due to increasing infiltration of slab-derived fluids/melts in the mantle wedge. Island arc tholeiitic and boninitic melts interacted with the residual harzburgites, leading to the formation of the mantle rocks in the north Tianshan ophiolite.

Acknowledgements

We would like to express our gratitude to Prof. Nelson Eby, Prof. Ibrahim Uysal, and an anonymous reviewer for constructive comments and suggestions, which helped us to improve this manuscript greatly. We are also grateful to Dr. Jiahao Zheng, who provided detailed comments on the early version of this manuscript. This study was supported by the Natural Science Foundation of China (Grant Nos. 41330210, 41672047).

Appendix A. Supplementary data

Supplementary data to this article can be found online at https://doi.org/10.1016/j.lithos.2018.08.012.

References

Abdel-Karim, A.A.M., Ali, S., Helmy, H.M., El-Shafei, S.A., 2016. A fore-arc setting of the Gerf ophiolite, Eastern Desert, Egypt: Evidence from mineral chemistry and geochemistry of ultramafites. Lithos 263, 52–65.

Ahmed, A.H., Surour, A.A., 2016. Fluid-related modifications of Cr-spinel and olivine from ophiolitic peridotites by contact metamorphism of granitic intrusions in the Ablah area, Saudi Arabia. Journal of Asian Earth Sciences 122, 58–79.

An, F., Zhu, Y.F., Wei, S.N., Lai, S.C., 2013. An Early Devonian to Early Carboniferous volcanic arc in North Tianshan, NW China: geochronological and geochemical evidence from volcanic rocks. Journal of Asian Earth Sciences 78, 100–113.

An, F., Zhu, Y.F., Wei, S.N., Lai, S.C., 2017. The zircon U-Pb and Hf isotope constraints on the basement nature and Paleozoic evolution in northern margin of Yili Block, NW China. Gondwana Research 43, 41–54.

Arai, S., Matsukage, K., Isobe, E., Vysotskiy, S., 1997. Concentration of incompatible elements in oceanic mantle: effect of melt/wall interaction in stagnant or failed melt conduits within peridotite. Geochimica et Cosmochimica Acta 61, 671–675.

Arculus, R.J., Ishizuka, O., Bogus, K.A., Gurnis, M., Hickey-Vargas, R., Aljahdali, M.H., Bandini-Maeder, A.N., Barth, A.P., Brandl, P.A., Drab, L., do Monte Guerra, R., Hamada, M., Jiang, F.Q., Kanayama, K., Kender, S., Kusano, Y., Li, H., Loudin, L.C., Maffione, M., Marsaglia, K.M., McCarthy, A., Meffre, S., Morris, A., Neuhaus, M., Savov, I.P., Sena, C., Tepley Iii, F.J., Vvan Dder Land, C., Yogodzinski, G.M., Zhang, Z. H., 2015. A record of spontaneous subduction initiation in the Izu-Bonin-Mariana arc. Nature Geoscience 8, 728–733.

Butler, J.P., Beaumont, C., 2017. Subduction zone decoupling/retreat modeling explains south Tibet (Xigaze) and other supra-subduction zone ophiolites and their UHP mineral phases. Earth and Planetary Science Letters 463, 101–117.

Chen, G.W., Deng, T., Xia, H., Liu, Q., 2012. Ocean island basalt associated with Bayingou ophiolite in West Tianshan Mountains: evidence from major and trace elements. Acta Petrologica et Mineralogica 31, 831–842 (in Chinese with English abstract).

Chen, Z.Q., Liao, Z.T., Liu, L.J., 2015. Correction of two Upper Paleozoic stratigraphic units in the Tianshan Mountains region, Xinjiang Uygur Autonomous Region and implications on the Late Paleozoic evolution of Tianshan tectonic complex, Northwest China. Journal of Palaeogeography 4, 358–370.

Cole, R.B., Stewart, B.W., 2009. Continental margin volcanism at sites of spreading ridge subduction: examples from southern Alaska and western California. Tectonophysics 464, 118–136.

Condie, K.C., 2005. High field strength element ratios in Archean basalts: a window to evolving sources of mantle plumes? Lithos 79, 491–504.

Czertowicz, T.A., Scott, J.M., Waight, T.E., Palin, J.M., Van der Meer, Q.H.A., Le Roux, P., Münker, C., Piazolo, S., 2016. The anita peridotite, New Zealand: ultra-depletion and subtle enrichment in sub-arc mantle. Journal of Petrology 57, 717–750.

Dai, J.G., Wang, C.S., Hébert, R., Santosh, M., Li, Y.L., Xu, J.Y., 2011. Petrology and geochemistry of peridotites in the Zhongba ophiolite, Yarlung Zangbo Suture Zone: implications for the Early Cretaceous intra-oceanic subduction zone within the Neo-Tethys. Chemical Geology 288, 133–148.

Dick, H.J.B., Bullen, T., 1984. Chromian spinel as a petrogenetic indicator in abyssal and Alpine-type peridotites and spatially associated lavas. Contributions to Mineralogy and Petrology 86, 54–76.

Dilek, Y., Furnes, H., 2011. Ophiolite genesis and global tectonics: geochemical and tectonic fingerprinting of ancient oceanic lithosphere. Geological Society of America Bulletin 123, 387–411.

Dilek, Y., Furnes, H., Shallo, M., 2007. Suprasubduction zone ophiolite formation along the periphery of Mesozoic Gondwana. Gondwana Research 11, 453–475.

Ferrari, L., Petrone, C.M., Francalanci, L., 2001. Generation of oceanic-island basalt-type volcanism in the western Trans-Mexican volcanic belt by slab rollback, asthenosphere infiltration, and variable flux melting. Geology 29, 507–510.

Green, T., Blundy, J.D., Adam, J., Yaxley, G.M., 2000. SIMS determination of trace ele-ment partition coefficients between garnet, clinopyroxene and hydrous basaltic liquids at 2-7.5 GPa and 1080–1200 °C. Lithos 53, 165–187.

Guo, L., Zhang, H.F., Harris, N., Pan, F.B., Xu, W.C., 2013. Late Cretaceous (~ 81 Ma) high-temperature metamorphism in the southeastern Lhasa terrane: implication for the Neo-Tethys ocean ridge subduction. Tectonophysics 608, 112–126.

Han, B.F., Guo, Z.J., Zhang, Z.C., Zhang, L., Chen, J.F., Song, B., 2010. Age, geochemistry, and tectonic implications of a late Paleozoic stitching pluton in the North Tian Shan suture zone, western China. Geological Society of America Bulletin 122, 627–640.

Ishii, T., Robinson, P.T., Maekawa, H., Fiske, R., 1992. Petrological Studies of Peridotites FromDiapiric Serpentinite Seamounts in the Izu-Mariana Fore-arc. In: Fryer, P., Pearce, J.A., Stokking, L.B. (Eds.), Leg 125 Proceedings of the Ocean Drilling Program, Scientific Results. vol. 125, pp. 445–485 College Station.

Jaques, A.L., Green, D.H., 1980. Anhydrous melting of peridotite at 0-15 kb pressure and the genesis of tholeiitic basalts. Contributions to Mineralogy and Petrology 73, 287–310.

Kapsiotis, A.N., 2013. Origin of mantle peridotites from the vourinos ophiolite complex, Greece, as deduced from Cr-spinel morphological and chemical variations. Journal of Geosciences 58, 217–231.

Khedr, M.Z., Arai, S., 2012. Petrology and geochemistry of prograde deserpentinized peridotites from Happo-O'ne, Japan: Evidence of element mobility during deserpentinization. Journal of Asian Earth Sciences 43, 150–163.

Khedr, M.Z., Arai, S., 2017. Peridotite-chromitite complexes in the Eastern Desert of Egypt: Insight into Neoproterozoic sub-arc mantle processes. Gondwana Research 52, 59–79.

Khogenkumar, S., Singh, A.K., Singh, R.B., Khanna, P.P., Singh, N.I., Singh, W.I., 2016. Coexistence of MORB and OIB-type mafic volcanics in the Manipur Ophiolite Complex, Indo-Myanmar Orogenic Belt, northeast India: implication for heterogeneous mantle source at the spreading zone. Journal of Asian Earth Sciences 116, 42–58.

Kinzler, R.J., 1997. Melting of mantle peridotite at pressures approaching the spinel to garnet transition: application to mid-ocean ridge basalt petrogenesis. Journal of Geophysical Research 102, 853–874.

Kinzler, R.J., Grove, T.L., 1992. Primary magmas of mid-ocean ridge basalts 1. Experiments and methods. J. Geophys. Res. Solid Earth 97, 6885–6906.

Leake, B.E., Woolley, A.R., Arps, C.E., Birch, W.D., Gilbert, M.C., Grice, J.D., Hawthorne, F.C., Kato, A., Kisch, H.J., Krivovichev, V.G., Linthout, K., Laird, J., Mandarino, J., Maresch, W. V., Nickel, E.H., Schumacher, J.C., Smith, D.C., Stephenson, N.C.N., Ungaretti, L., Whittaker, E.G.J.W., Youzhi, G., 1997. Nomenclature of amphiboles: report of the subcommittee on amphiboles of the international mineralogical association commission on new minerals and mineral names. Mineralogical Magazine 61, 295–321.

Li, C., Xiao, W.J., Han, C.M., Zhou, K.F., Zhang, J.E., Zhang, Z.X., 2015. Late Devonian-early Permian accretionary orogenesis along the North Tianshan in the southern Central Asian Orogenic Belt. International Geology Review 57, 1023–1050.

Loucks, R.R., 1990. Discrimination of ophiolitic from nonophiolitic ultramafic-mafic allochthons in orogenic belts by the Al/Ti ratio in clinopyroxene. Geology 18, 346–349.

Marchesi, C., Garrido, C.J., Proenza, J.A., Hidas, K., Varas-Reus, M.I., Butjosa, L., Lewis, J.F., 2016. Geochemical record of subduction initiation in the sub-arc mantle: Insights from the Loma Caribe peridotite (Dominican Republic). Lithos 252, 1–15.

Matsumoto, I., Arai, S., 2001. Morphological and chemical variations of chromian spinel in dunite-harzburgite complexes from the Sangun zone (SW Japan): implications for mantle/melt reaction and chromitite formation processes. Mineralogy and Petrology 73, 305–323.

Morishita, T., Dilek, Y., Shallo, M., Tamura, A., Arai, S., 2011. Insight into the uppermost mantle section of a maturing arc: the Eastern Mirdita ophiolite, Albania. Lithos 124, 215–226.

Nozaka, T., 2003. Compositional heterogeneity of olivine in thermally metamorphosed serpentinite from Southwest Japan. American Mineralogist 88, 1377–1384.

Parkinson, I.J., Pearce, J.A., 1998. Peridotites from the Izu-Bonin-Mariana fore-arc (ODP Leg125): evidence for mantle melting and melt–mantle interaction in a suprasubduction zone setting. Journal of Petrology 39, 1577–1618.

Pearce, J.A., 2008. Geochemical fingerprinting of oceanic basalts with applications to ophiolite classification and the search for Archean oceanic crust. Lithos 100, 14–48.

Pearce, J.A., 2014. Immobile element fingerprinting of ophiolites. Elements 10, 101–108.

Pearce, J.A., Peate, D.W., 1995. Tectonic implications of the composition of volcanic arc magmas. Annual Review of Earth and Planetary Sciences 23, 251–285.

Pearce, J.A., van der Laan, S.R., Arculus, R.J., Murton, B.J., Ishii, T., Peate, D.W., Parkinson, I.J., 1992. 38. Boninite and harzburgite from Leg 125 (Bonin-Mariana Forearc): a case study of magma genesis during the initial stages of subduction. Proceeding of the Ocean Drilling Program, Scientific Results 125, 623–659.

Pearce, J.A., Barker, P.F., Edwards, S.J., Parkinson, I.J., Leat, P.T., 2000. Geochemistry and tectonic significance of peridotites from the South Sandwich arc-basin system, South Atlantic. Contributions to Mineralogy and Petrology 139, 36–53.

Qiu, T., Zhu, Y.F., 2018. Listwaenite in the Sartohay ophiolitic mélange (Xinjiang, China): A genetic model based on petrology, U-Pb chronology and trace element geochemistry. Lithos 302, 427–446.

Reagan, M.K., Ishizuka, O., Stern, R.J., Kelley, K.A., Ohara, Y., Blichert-Toft, J., Bloomer, S.H., Cash, J., Fryer, P., Hanan, B.B., Hickey-Vargas, R., Ishii, T., Kimura, J.-I., Peate, D.W.,

Rowe, M.C., Woods, M., 2010. Fore-arc basalts and subduction initiation in the Izu-Bonin-Mariana system. Geochemistry, Geophysics, Geosystems 11 (3). https://doi.org/10.1029/2009gc002871.
Saccani, E., Dilek, Y., Photiades, A., 2017. Time-progressive mantle-melt evolution and magma production in a Tethyan marginal sea: A case study of the Albanide-Hellenide ophiolites. Lithosphere https://doi.org/10.1130/L602.1.
Saka, S., Uysal, I., Akmaz, R.M., Kaliwoda, M., Hochleitner, R., 2014. The effects of partial melting, melt-mantle interaction and fractionation on ophiolite generation: Constraints from the late Cretaceous Pozantı-Karsantı ophiolite, southern Turkey. Lithos 202, 300–316.
Seyler, M., Lorand, J.P., Dick, H.J.B., Drouin, M., 2007. Pervasive melt percolation reactions in ultra-depleted refractory harzburgites at the Mid-Atlantic Ridge, 15° 20′N: ODP Hole 1274A. Contributions to Mineralogy and Petrology 153, 303–319.
Shaw, D.M., 2000. Continuous (dynamic) melting theory revisited. The Canadian Mineralogist 38, 1041–1063.
Shervais, J.W., 1982. Ti-V plots and the petrogenesis of modern and ophiolitic lavas. Earth and Planetary Science Letters 59, 101–118.
Shervais, J.W., 2001. Birth, death, and resurrection: the life cycle of suprasubduction zone ophiolites. Geochemistry, Geophysics, Geosystems 2. https://doi.org/10.1029/2000gc000080.
Stern, R.J., Reagan, M., Ishizuka, O., Ohara, Y., Whattam, S., 2012. To understand subduction initiation, study forearc crust: To understand forearc crust, study ophiolites. Lithosphere 4, 469–483.
Suhr, G., 1999. Melt migration under oceanic ridges: inferences from reactive transport modelling of upper mantle hosted dunites. Journal of Petrology 40, 575–599.
Sun, S.S., McDonough, W.S., 1989. Chemical and isotopic systematics of oceanic basalts: implications for mantle composition and processes. Geological Society, London, Special Publications 42, 313–345.
Takahashi, E., Uto, K., Schilling, J.G., 1987. Primary magma compositions and Mg/Fe ratios of their mantle residues along mid-Atlantic ridge 29N to 73N Technical Report, A9. Institut of Studies Earth's Interior, Okayama University Series, pp. 1–14.
Tamura, A., Morishita, T., Ishimaru, S., Hara, K., Sanfilippo, A., Arai, S., 2016. Compositional variations in spinel-hosted pargasite inclusions in the olivine-rich rock from the oceanic crust-mantle boundary zone. Contributions to Mineralogy and Petrology 171, 39.
Tang, G.J., Wang, Q., Wyman, D.A., Li, Z.X., Xu, Y.G., Zhao, Z.H., 2012. Metasomatized lithosphere–asthenosphere interaction during slab roll-back: evidence from Late Carboniferous gabbros in the Luotuogou area, Central Tianshan. Lithos 155, 67–80.
Uysal, I., Ersoy, E.Y., Karsli, O., Dilek, Y., Sadiklar, M.B., Ottley, C.J., Tiepolo, M., Meisel, T., 2012. Coexistence of abyssal and ultra-depleted SSZ type mantle peridotites in a Neo-Tethyan ophiolite in SW Turkey: constraints from mineral composition, whole-rock geochemistry (major-trace-REE-PGE), and Re-Os isotope systematics. Lithos 132-133, 50–69.
Uysal, I., Ersoy, E.Y., Dilek, Y., Escayola, M., Sarıfakıoğlu, E., Saka, S., Hirata, T., 2015. Depletion and refertilization of the Tethyan oceanic upper mantle as revealed by the early Jurassic Refahiye ophiolite, NE Anatolia-Turkey. Gondwana Research 27, 594–611.
Uysal, I., Ersoy, E.Y., Dilek, Y., Kapsiotis, A., Sarıfakıoğlu, E., 2016. Multiple episodes of partial melting, depletion, metasomatism and enrichment processes recorded in the heterogeneous upper mantle sequence of the Neotethyan Eldivan ophiolite, Turkey. Lithos 246, 228–245.
Wang, B., Faure, M., Cluzel, D., Shu, L.S., Charvet, J., Meffre, S., Ma, Q., 2006. Late Paleozoic tectonic evolution of the northern West Chinese Tianshan belt. Geodinamica Acta 19, 237–247.
Whattam, S.A., Stern, R.J., 2011. The 'subduction initiation rule: a key for linking ophiolites, intra-oceanic forearcs, and subduction initiation. Contributions to Mineralogy and Petrology 162, 1031–1045.
White, W.M., 2010. Oceanic island basalts and mantle plumes: the geochemical perspective. Annual Review of Earth and Planetary Sciences 38, 133–160.
Workman, R.K., Hart, S.R., 2005. Major and trace element composition of the depleted MORB mantle (DMM). Earth and Planetary Science Letters 231, 53–72.
Wu, J.Y., Liu, C.D., 1989. Geological features of Bayingol ophiolitic suite of North Tianshan, Xinjiang. Acta Petrologica Sinica 2, 76–88 (in Chinese with English abstract).
Xia, L.Q., Li, X.M., Xu, X.Y., Xia, Z.C., Ma, Z.P., Wang, L.S., 2005. Petrogenetic evolution of the Bayan Gol ophoilite-Geological record of an Early Carboniferous "Red Sea type" ocean basin in the Tianshan Mountains, Northwestern China. Acta Geologica Sinica (English Edition) 79, 174–192.
Xiao, X.C., Tang, Y.Q., Feng, Y.M., Zhu, B.Q., Li, J.Y., Zhao, M., 1992. Tectonic evolution of Northern Xinjiang and its adjacent regions: Beijing. Geological Publishing House (169 p. in Chinese with English abstract).
Xu, X.Y., Li, X.M., Ma, Z.P., Xia, L.Q., Xia, Z.C., Peng, S.X., 2006. LA-ICPMS zircon U-Pb dating of gabbro from the Bayingou ophiolite in the Northern Tianshan mountains. Acta Geologica Sinica 8, 1168–1176 (in Chinese with English abstract).
Yang, G.X., Li, Y.J., Xiao, W.J., Tong, L.L., 2015. OIB-type rocks within West Junggar ophiolitic mélanges: Evidence for the accretion of seamounts. Earth-Science Reviews 150, 477–496.
Yang, G.X., Li, Y.J., Kerr, A.C., Tong, L.L., 2018. Accreted seamounts in North Tianshan, NW China: Implications for the evolution of the Central Asian Orogenic Belt. Journal of Asian Earth Sciences 153, 223–237.
Zhang, Z.H., Wang, Z.L., Du, A.D., Zuo, G.C., Liu, M., Wang, L.S., Wang, J.W., 2008. Tectonic setting of the volcanic rocks in Dabate district and their constraints on the ore-forming of porphyry ore, West Tianshan Mountains. Acta Geologica Sinica 82, 1494–1503 (in Chinese with English abstract).
Zhang, H.C., Zhu, Y.F., Feng, W.Y., Tan, Y.W., An, F., Zheng, J.H., 2017. Paleozoic intrusive rocks in the Nalati mountain range (NMR), southwest Tianshan: geodynamic evolution based on petrology and geochemical studies. Journal of Earth Science 28, 196–217.
Zhao, Z.H., Wang, Q., Xiong, X.L., Niu, H.C., Zhang, H.X., Qiao, Y.L., 2007. Magnesian igneous rocks in northern Xinjiang. Acta Petrologica Sinica 23, 1696–1707 (in Chinese with English abstract).
Zhu, Y.F., Ogasawara, Y., 2002. Carbon recycled into the deep Earth: Evidenced by dolomite dissociation in subduction-zone rocks. Geology 30, 947–950.
Zhu, Y.F., Sun, S.H., Gu, L.B., Ogasawara, Y., Jiang, N., Honma, H., 2001. Permian volcanism in the Mongolian orogenic zone, northeast China: geochemistry, magma sources and petrogenesis. Geological Magazine 138, 101–115.
Zhu, Y.F., Zhang, L.F., Gu, L.B., Guo, X., Zhou, J., 2005. The zircon SHRIMP chronology and trace element geochemistry of the Carboniferous volcanic rocks in western Tianshan Mountains. Chinese Science Bulletin 50, 2201–2212.
Zhu, Y.F., Guo, X., Song, B., Zhang, L.F., Gu, L.B., 2009. Petrology, Sr-Nd-Hf isotopic geochemistry and zircon chronology of the Late Palaeozoic volcanic rocks in the southwestern Tianshan Mountains, Xinjiang, NW China. Journal of the Geological Society, London 166, 1085–1099.
Zhu, Y.F., An, F., Feng, W.Y., Zhang, H.C., 2016. Geological Evolution and Huge Ore-Forming Belts in the Core Part of the Central Asian Metallogenic Region. Journal of Earth Science 27, 491–506.